Rodrigo Miguel M. Ribeiro

Bachelor in Micro and Nanotechnologies Engineering

Development of a lift-off process for sub-micrometer structures implemented on ultra-thin film Cu(In,Ga)Se_2 (CIGS) solar cells

Dissertation submitted in partial fulfillment of the requirements for the degree of:

Master of Science in

Micro and Nanotechnology Engineering

Supervisor: Doctor Paulo Fernandes, Cooperation Associate, International Iberian Nanotechnology Laboratory and Adjunct Professor, Dept of Physics School of Engineering of Porto Polytechnic.

Co-Supervisor: Doctor Hugo Águas, Associate Professor, Faculty of Sciences and Technology, New University of Lisbon.

Examination Committee:

Chairperson:

Rapporteurs:

FACULDADE DE CIÊNCIAS E TECNOLOGIA
UNIVERSIDADE NOVA DE LISBOA

October, 2019

Development of a lift-off process for sub micrometer structures implemented on ultra-thin film Cu(In,Ga)Se2 (CIGS) solar cells

“What is research but a blind date with knowledge?”

Will Harvey

Acknowledgments

This work was the final step on a journey started 5 years ago that is now reaching its end. The memories created and the friends I have found along the way, will fill me with an everlasting feeling of joy. Therefore, in this section, I would like to thank everyone that somehow contributed to my success.

Primeiramente gostaria de agradecer, ao Prof. Dr. Rodrigo Martins e à Prof. Dr. Elvira Fortunato, pela oportunidade única que me deram a mim e a tantos outros, através da criação do curso de Engenharia em Micro e Nanotecnologias, curso ímpar em Portugal. É realmente um privilégio adquirir conhecimento tão inovador e poder estar em contacto com equipamentos vanguardistas.

Ao meu orientador, Prof. Dr. Paulo Fernandes e ao Group Leader que me acolheu no INL, Prof. Dr. Pedro Salomé, um especial obrigado. Sem vocês, sem a vossa orientação diária e os insights valiosos este trabalho jamais teria sido possível realizar. É importante valorizar o trabalho feito no grupo. Um trabalho de grande qualidade, num grupo com vários estudantes de doutoramento, que graças ao Paulo e ao Pedro, têm a oportunidade de ter uma formação, que aos meus olhos me parece única, com um acompanhamento excecional e que também comigo foi partilhado. Por tudo isso, mais uma vez, um grande obrigado!

Ao meu co-orientador, Prof. Dr. Hugo Águas, agradeço por todo o trabalho realizado, arranjando aos alunos do nosso curso excelentes oportunidades para quem procura fazer a tese fora da nossa faculdade.

A todo o staff de sala limpa no INL que de uma forma ou de outra me ajudou no decorrer deste trabalho, em especial ao Paulo Coelho e ao Pedro Anacleto, um grande obrigado.

To my colleagues and friends in the NOA group, this part is for you guys. Jennifer, Marco, Miguel, e Tomás, vocês são espetaculares. Eu sei que sou um chato primeira e só o facto de me conseguirem aturar todos os dias já era uma vitória. Mas não, por cima disso ainda tenho o privilégio de que me encham de ensinamentos e que me corrijam a tese. Não há palavras para vos agradecer. André Célia, Filipe, João e Maria vocês sem saberem passaram meses a ensinar-me. Só o facto de me fazerem perguntas sobre algo que à primeira vista parecia simples e que depois me apercebia que nem eu tinha a resposta, fazia com que eu tivesse que ir à procura dessa mesma resposta com vocês. Por isso, um grande obrigado! Olivier, you are the best. The things you can do with a SEM are unbelievable. For all the images you took during my stay at INL and your everlasting good mood, a special thanks. Evelina and Ronja, I must admit I am a bit afraid of the Swedes nowadays. Are they all, like you two? Thank you for your awesomeness! I will miss you both. Finalmente, para o meu colega de trabalho e de casa, Tó, se tu fosses mais rápido tínhamos conseguido fugir. Tirando isso, obrigado por toda a ajuda, as nossas discussões acerca da teoria por detrás dos resultados que íamos obtendo foram importantes e de certa forma deixavam-me sempre mais descansado.

Aos meus coleguinhas de casa Bracarenses, António, João, Pedro e Sara, e à menina Beatriz, posteriormente adotada, um especial obrigado. Malta, estar em Braga foi fácil. Acho que isso foi graças a vocês.

Aos amigos do chat, Bernardo, João, Matinhos Matex, Saraiva, Simão, Nuno, obrigado por estes 5 anos. Vão deixar saudades. Aos amigos do chat original, Diogo, Fred, Guilherme e Ricardo, um obrigado especial. Paciência infinita é um ensinamento que vou levar para a vida.

Aos amigos de longa data, Ana, Chico, Gui, Mariana, Miguel, Ricardo, Rocha e Tiago, queria também deixar um agradecimento especial. Vocês são um dos pilares fundamentais da minha vida.

Por fim, o maior agradecimento vai para as pessoas a quem devo mais, meus pais e irmã, sem vocês nada disto era possível.

Abstract

Cu(In,Ga)Se_2 (CIGS) solar cells have been gathering increased attention by the scientific and the industrial community, with values of efficiency reaching a record value of 23.35%. Nevertheless, the use of the scarce elements as In and Ga might translate into a higher production cost in the near future. The reduction of the absorber thickness is a solution to this problem. However, some studies point that for sub-micrometer thicknesses, rear contact recombination vastly increases, and the light absorption is incomplete. In order to tackle these problems, several passivation and optical techniques are being developed.

The focus of this thesis is to develop a lift-off process for the implementation of a novel structure with the objective of increasing the optical reflection on the rear contact, increasing the optical path. The structure consisted on a metal/dielectric stack patterned with Mo lines that will make the electrical contact with CIGS. Through the use of several metals (Pd, Pt, Cu, Ta) encapsulated with a dielectric layer (SiO_2), that were then patterned with Mo lines, using a lithographic step, we managed to enhance both External Quantum Efficiency and the Short Circuit Current (4.13 mA/cm_2 abs. increase) on the modified CIGS solar cells, in comparison to an ultrathin reference.

Keywords: CIGS, Solar cells, Optical reflection, Lift-off

Resumo

As células solares de $Cu(In,Ga)Se_2$ (CIGS) têm sido objeto de atenção tanto por parte da comunidade científica como da indústria, com valores de eficiência a chegarem a valores recorde de 23.35%. No entanto, a utilização de elementos raros como o In e o Ga, podem levar a que a sua produção tenha um custo mais elevado, quando comparado com outras tecnologias. Uma possível solução para este problema passa pela redução da camada CIGS. O desafio é conseguir que a diminuição desta camada não influencie a eficiência da célula como um todo, estando reportados em alguns estudos a existência do aumento da recombinação no contacto traseiro e de uma absorção de luz incompleta. Uma forma de resolver estes problemas consiste no desenvolvimento de novas técnicas óticas e de passivação, que permitam aumentar a quantidade de luz absorvida.

O objetivo desta tese passa pelo desenvolvimento de um processo de lift-off que permita a introdução de uma estrutura inovadora no contacto traseiro de células solares CIGS ultrafinas, aumentando assim a reflexão ótica e consequentemente a sua eficiência. A estrutura consiste na utilização de uma dupla camada de metal/diétrico que é consequentemente padronizada com linhas de Mo e que possibilitam o contacto elétrico com o CIGS. Através da utilização de vários metais (Pd, Pt, Cu, Ta) encapsulados com uma camada dielétrica (SiO_2), posteriormente padronizada com as linhas de Mo usando um processo litográfico, foi nos possível aumentar a eficiência quântica externa e a corrente de curto circuito (aumento de 4.25 mA/cm_2) nas células solares de CIGS modificadas.

Palavras-chave: CIGS, células solares, reflexão ótica, Lift-off.

Contents

List of Figures

List of Tables

Symbol	Name	Unit
Al_2O_3	Aluminium Oxide	
Au	Gold	
c	Free space light speed	m/s
Cu	Copper	
D	Displacement fields	C/m^2
e	Electronic charge	C
E	Electrical fiel	V/m
$\|E\|^2$	Electrical field intensity	V/m^2
FF	Fill-factor	%
Ga	Galium	
H	Magnetic fields	A/m
h	Planck constant	
In	Indium	
$I_{AM1.5}$	AM 1.5 Intensity	$W/m^2 \cdot m^1$
J	Current density	A/m^2
j_0	Saturation current density	A/m^2
J_{SC}	Short-circuit current density	A/m^2
k	Boltzmann's constant	J/K
Mo	Molybdenum	
n	Ideality factor	%
$PMMA$	Polymethyl methacrylate	
P_{ABS}	Power absorbed per unit volume	
T	Temperature	K
SiO_2	Silicon oxide	
Ta	Tantalum	
V_D	Applied voltage across the diode	V
V_{OC}	Open-circuit voltage	V
ω	Angular frequency	rads/s
η	Power conversion efficiency	%
ϵ''	Imaginary part of the dielectric permittivity	F/m
$\epsilon_\gamma(\omega)$	Complex relative dielectric constant	
ϕ	Photon flux	

Acronyms

AFM	Atomic Force Microscopy
Al:ZnO	Aluminium doped zinc oxide
CBD	chemical bath deposition
CIGS	Copper Indium Gallium Diselenide $Cu(In,Ga)Se_2$
DWL	direct writing laser
EQE	External quantum efficiency
FDTD	Finite-Difference Time
INL	International Iberian Nanotechnology Laboratory
i-ZnO	Intrinsic zinc oxide
PV	Photovoltaic
RIE	reactive ion etching
SEM	Scanning Electron Microscopy
SLG	soda lime glass
TCO	transparent conducting oxide

Motivation

Since the beginning of the human species, mankind has searched for new ways to produce energy. Most of the times that a new way of energy was found, it led to a rapid evolution in the field of technology. An easy example of that is the industrial revolution in the transition from the XVIII to the XIX century that started in Great Britain with the burning of fossil fuels. Despite the major progress made thanks to this source of energy and the fact that remains the one that is used the most, we have come to the realization that it has its limitations. The first one is related with the fact that is a finite resource. The second one, and most important, is that burning fossil fuels jeopardizes the health of the world we live in. Regarding this, new non-polluting and renewable sources of energy have been developed to suppress the problems associated with the one referred above. It is in this field of research that Photovoltaics grow.

Through the Photovoltaic effect, first seen in 1839 by Alexander-Edmond Becquerel, it is possible to a material to absorb sunlight and convert it into electricity, and we know that sun radiates more than enough energy to suppress the human needs each day. Taking this into account, we can see that the potential of PV technology is huge, although some issues still seek a solution. For example, the power conversion efficiency of solar cells remains one of the main focus of investigation across the world and despite the frequent improvements, further research is needed considering that none of the theoretical limits described by Shockley and Queisser (1961) for solar cells based in p-n junctions has yet been reached.[1]

Solar cells based on the PV effect described above are well established in the market of energy, having attained an exponential growth since the beginning of the decade. According to the *World Energy Outlook*, in 2015, a major milestone was achieved when renewable sources exceeded the energy produced by nuclear and fossil fuels.[2]

More recently new developments have been made in the field by introducing thin film solar cells (TFSC). There are three main technologies of TFSC: amorphous Silicon (a-Si), copper indium gallium selenide (CIGS) and cadmium telluride (CdTe), with respectively record efficiencies (at a laboratory level) of 14.0%, 22.9% and 21.0%[3]. With this type of cells, it is possible to diminish the quantity of material used in the production and, therefore, reduce its cost even though they have a deficit in terms of efficiency when compared with the conventional solar cells. The reduction in efficiency is related to an increase in recombination and a decrease in light absorption. Both effects associated with the reduced thickness of these cells. Bearing this, the research done nowadays aims to find an equilibrium between thickness, efficiency, and cost of production.

1.1 Solar Cells

1.1.1 Device physics

Solar cells are optoelectronic devices based on semiconductors that make use of the photovoltaic effect to convert sunlight into electricity. Two types of doped semiconductors can be defined. The first, has the addition of certain impurities (atoms) to its lattice, while the second is intrinsically doped, just by the way atoms are arranged (CIGS case). Through doping it is possible to modify a semiconductor's electrical properties, leading to a material that can either be a p-type or a n-type (depending if it has an increased concentration of holes or electrons). When these two different types of doped materials are brought together, they form a P-N junction, the basis of solar cells. P-N junctions can be sub-divided in two categories: homojunctions and heterojunctions. In the first case, the junction is formed by the same material, with different dopants, granting the n and p-type characteristics. In heterojunctions, the used semiconductors are different.[4], [5]

As depicted in **Figure 1.1**, when a p-n junction is formed, a depletion region (or space charge region) appears associated with the diffusion of positive carriers from the p to the n-type and the negative carriers from the n to the p-type material. This depletion region, through static charges, gives rise to a built-in electric field near the interface that will separate the electron-hole pairs created by the incident photons on the solar cell, thus leading to the generation of electric current.[4]

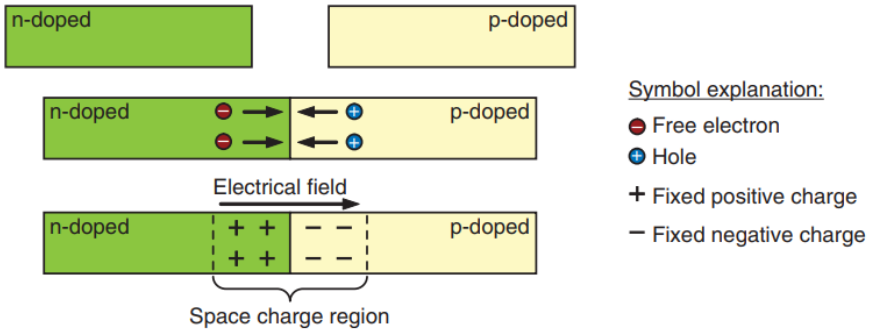

Figure 1.1 – Schematic of the formation of the space charge region. Taken from [1].

1.1.2 Single diode model and electrical characterization parameters

The single diode model is one of the simplest approaches to represent the basic principles of operation of a solar cell from an electrical standpoint.

In a diode, when an external bias is applied, the barrier that blocks electrons from flowing from the n to the p-type material drops, leading to the generation of current density (J) [6]:

$$J = j_0 \left[exp\left(\frac{qV_D}{nkT}\right) - 1 \right] \tag{1}$$

where, j_0 represents the saturation current density, q the electron charge, V_D the bias applied to the diode, n the ideality factor, k the Boltzmann's constant and T the temperature of the device.

In the case of a solar cell, it is right to assume that it behaves like a diode when it is in dark and as a non-ideal diode that generates a current, J_L, when under illumination [6]:

$$J = j_0 \left[exp\left(\frac{qV_D}{nkT}\right) - 1 \right] + \frac{V - JR_S}{R_{SH}} - J_L \tag{2}$$

Equation 2 provides a more accurate behavior of a solar cell, in comparison with **equation 1**. The reason for that is related with the appearance of a series resistance, R_S, a shunt resistance, R_{SH}, and J_L, the photogenerated current density. R_S have two main origins: **i,** the intrinsic resistance that the current flowing through the semiconductor and the metal contacts encounters; **ii,** the resistance found in the interface with the contacts. while R_{SH} is related to "alternative paths" that circumvent the p-n junction to where the current flow, leading to a decrease on the photogenerated current. Ideally, R_S should be 0 while R_{SH} should be maximized in order to mitigate the resistive losses referred before. Both these resistances are directly related with the Fill Factor (FF) that will be discussed later.[7]

By using the **equation 2**, it is possible to draw the current density-voltage (J-V) curve of a solar cell, both in dark and under illumination (solar spectrum at 25ºC - A.M 1.5 (**Figure 1.2**). From the J-V curve, some important parameters can be extracted such as: i) the open-circuit voltage, V_{oc}, ii) the J_{sc}, short circuit current, iii) the maximum point of voltage and current, V_{MP} and J_{MP}, respectively.[6]

FF depicts the relation between the maximum power and the product of V_{oc} and J_{sc}. This parameter is represented by the following equation and, in an ideal world, it would be 1 [8]:

$$FF = \frac{V_{MP}J_{MP}}{V_{oc}J_{SC}} \tag{3}$$

However, when referring to solar cells, from an electrical point of view, the most important parameter to evaluate its performance (that can be taken from a J-V curve) is the light to power conversion efficiency (η), represented by [6]:

$$\eta = \frac{P_{out}}{P_{in}} = \frac{V_{MP}J_{MP}}{P_{in}} = \frac{V_{OC}J_{SC}FF}{P_{in}} \tag{4}$$

where the ratio between the amount of energy that reaches the cell in the form of light and the energy output that the cell produces can be calculated.

Quantum efficiency is another relevant parameter for solar cells characterization. It can be separated into external QE (EQE) and internal QE (IQE). EQE represents the ratio between the number of charge carriers collected and the number of incident photons at a certain wavelength, while IQE is the ratio between the number of charge carriers collected and the number of photons that are absorbed by the solar cell, i.e reflection of the device excluded. Moreover, EQE can also provide a bandgap estimative for the layers in the solar cell as well as the J_{SC} of the device.[9]

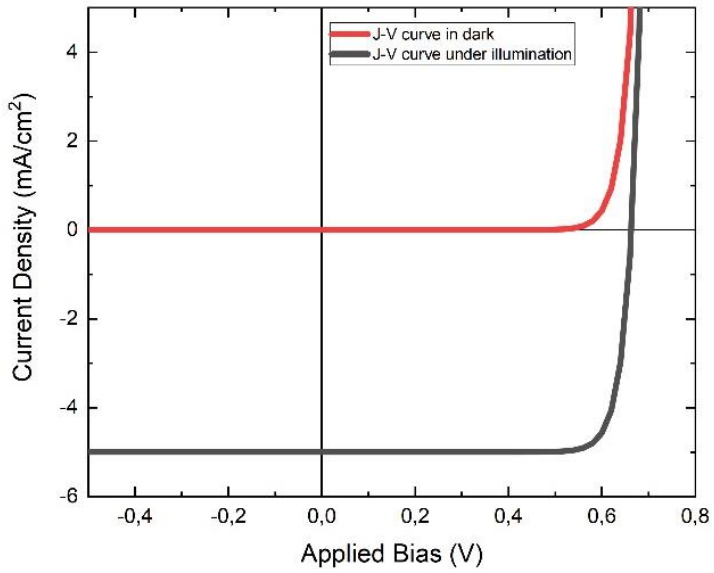

Figure 1.2 – Typical J-V curve of a solar cell.

1.2 CIGS Thin Film Solar Cells

1.2.1 State of the art

In 1975, a team of scientists from Bell Laboratories created the first CIGS solar cell with an efficiency of 12% by evaporating a layer of CdS on top of a $CuInSe_2$ crystal[10]. The first step towards a series of improvements had just been given. By the early 1980s, two deposition methods were being studied, co-evaporation and deposition-reaction. In 1982, Mickelsen and Chen, from Boeing, fabricated the first thin-film solar cell reaching an efficiency superior to 10% by using the co-evaporation technique to deposit the CIGS absorber layer. At the same time, Arco Solar used the deposition-reaction method employing Cu and In, as precursors, together with H_2Se. For many years, the deposition-reaction method gave much better results in terms of efficiency. The reaction process, where the use of Na allowed for better performances - even though that by that time the community did not know why. In the following years, when the use of glass as a substrate started to be standard, both methods above became equally good, delivering an efficiency of around 14%.[7, 8]. The improvement of the co-evaporation method, in particular, the development of the three-stage process, by the National Renewable Energy Laboratories (NREL), in 1994, led to the idea that reducing the CIGS layer was possible. The CIGS solar cell thickness reduction allowed for the CIGS technology to compete with the most promisor technologies at the time.

In 1997 and 1998, the first studies regarding ultra-thin CIGS solar cells appeared, both in USA and Japan. In this early stage, the main problems related with the shrinkage of the absorber (recombination and optical losses) came into view. Ever since these losses have been studied essentially by European groups[13].

Nowadays, the record for CIGS thin-film solar cells (TFSC) belongs to Solar Frontier, with an efficiency of 23.35% [14], while the record for CIGS ultra-thin fin solar cells (UTFSC) is detained by NREL, with an efficiency of 15.2% [15].

1.2.2 Typical structure

The typical structure of a CIGS thin-film solar cell is schematized in **Figure 1.3**. All the distinct represented layers are usually used by every laboratory or company that produces this type of cells.

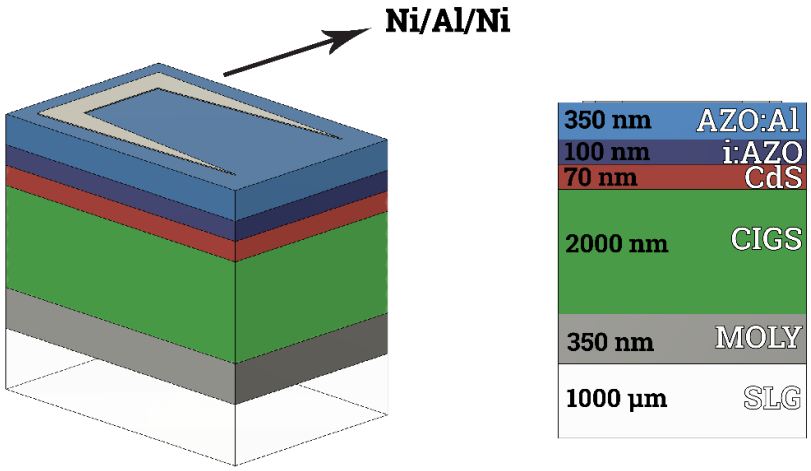

Figure 1.3 - Typical structure of a CIGS solar cell

The reasons why Soda Lime Glass (SLG) is used as substrate in standard CIGS solar cells are many: **i)** it is cheap, making it a viable option to large scale production; **ii)** it has a smooth surface; **iii)** is thermally stable and chemically inert; and **iv)** its thermal expansion coefficient is identical to the one of the CIGS. Furthermore, it still gives the possibility to supply sodium (Na) to the absorber layer, which is proven to enhance the CIGS solar cell electrical performance through passivation.[16], [17]

For the rear contact, molybdenum (Mo) is commonly used. Mo is known to create a quasi-ohmic contact with CIGS, promoted by the formation of a thin $MoSe_2$ layer[18]. Moreover, Mo is permeable to alkali elements, allowing for their diffusion. Previous studies showed that a bilayer of Mo is the best

approach to get a cell with superior quality[18]. The first layer is deposited at high pressure since it promotes a better adhesion to the SLG. In the second layer, a lower pressure is used because those conditions allow an increase in the conductance of the Mo.[18]

The CIGS absorber layer will be discussed later in chapter 2.3.

A great amount of investigation has been done when it comes to the buffer layer. Nowadays, the material of choice is Cadmium Sulfide (CdS), deposited by chemical bath deposition (CBD). CdS is known to create an excellent contact with the p-type CIGS maintaining an interface with a low defect density. On top of that, allows a steady change in the bandgaps (band-alignment) from the absorber layer to the TCO, increasing V_{OC} significantly. Nevertheless, Cds still presents some drawbacks and the pursuit of alternative materials for the buffer layer remains a key point in the CIGS solar cells research. CdS has a relative low bandgap (2.4eV) [19] that can lead to parasitic absorption at low wavelengths. Furthermore, Cd represents a hazard to both humans and the environment because of its extreme toxicity. The deposition method (CBD) used, that it is liquid-based, can be a problem when it comes to mass production since it represents the only step in the fabrication of a CIGS solar cell that cannot be done in vacuum.[19], [20]

The window layer stack is normally composed by two transparent layers: the shunt preventing layer and the front contact. The first layer is typically made of i:ZnO and it is used to improve device performance by reducing shunt currents and electrical inhomogeneities over the device area, at the same time, it protects the CIGS layer, against the sputtering deposition of the remaining layers. The second is usually ZnO:Al and its role is to enable the passage and collection of light. For this to be possible, the material chosen needs to have a high lateral conductivity in order to reduce resistive losses.[21]

The grid is usually made with a stack of Ni/Al/Ni and it is used only in research cells with the objective to make the electrical measurements and extract the parameters desired. This layer reduces the resistive losses, but the downside is that also increases the shadowing effect on the cell.[22]

1.2.3 Material

Copper indium gallium selenide (CIGS) is a p-type material belonging to the chalcogenide's group (**figure 1.4**) and based on two ternary chalcopyrite compounds: $CuInSe_2$ and $CuGaSe_2$ (I-III-IV semiconductors).[23]

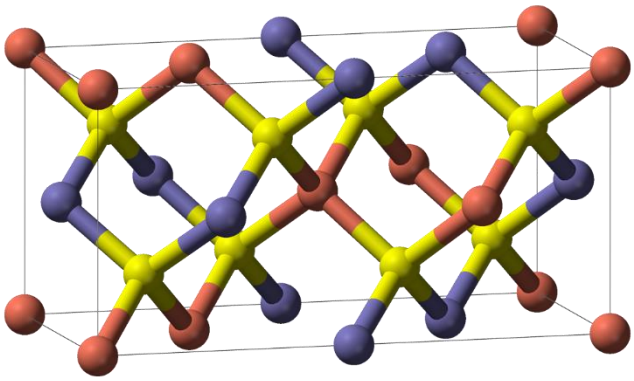

Figure 1.4 - The crystal structure of CIGS. The red atoms represent copper, the yellow ones, selenium, and the blue can either be indium or gallium.

This alloy is known for its direct bandgap, a high absorption coefficient (10^5 cm^{-1}) [19] and long-term stability providing an excellent alternative to the absorber layer when in comparison with silicon solar cells[24]. Direct bandgap semiconductors have the capability to absorb the same amount of light as indirect bandgap semiconductors with a substantially thinner layer. Moreover, CIGS has a tunable bandgap as function of the composition. By varying the amount of Ga, defined by the ratio (In/Ga), the bandgap can be changed between 1.04 and 168 eV. Another important aspect is the role of copper (Cu) in the chalcopyrite structure. It is known that Cu rich CIGS tend to grow bigger grains, leading to an increase in the crystalline properties. Nonetheless, in those materials, and considering that

they are self-doping semiconductors, the electrical performance is worse since they depend on Cu vacancies to develop their p-type behavior.[25]

1.2.4 Limitations of ultra-thin CIGS solar cells and optimization techniques

Standard CIGS solar cells require an approximate absorber thickness between 1 to 3 microns in order to efficiently absorb all the photons from incident light.[12] Research is now moving towards thinner absorbers, paving the way to the decrease of fabrication costs, and consequently, to cheaper renewable energy.[26] Nonetheless, some problems arise with the reduction of the CIGS thickness.[23] The deficient absorption of light is reported by some studies.[27], [28] By decreasing the thickness of the absorber layer, the optical path decreases accordingly, therefore leading to a loss in efficiency. Another relevant problem is the back-contact recombination. Through the reduction of the solar cell absorber, the electron-hole pairs will be separated closer to the back contact, hence increasing the possibility of recombination.

In order to tackle these problems, some groups have tried to use new approaches such as the use of a passivation layer, or through light management techniques.

1.2.4.1 Passivation effects

Impurities and defects are present in the lattice of semiconductors. Nonetheless, in the case of ultra-thin film solar cells, it is in the interface of the material where most of the recombination normally happens. Many of the cells fabricated nowadays rely in a bandgap engineering by a Ga grading to solve this problem. More recently, some groups have studied a way to reduce these losses. Salomé *et. al.* used a dielectric as a passivation layer with nanostructured point contacts in the rear to increase performance of the solar cell. This improvement is based in two effects [29]:

- **Chemical passivation** - With the abrupt disruption of the crystal lattices (interface), dangling bonds (e.g. Se vacancies) tend to appear, thus increasing recombination sites. Chemical passivation results from the bonding between the dielectric layer and the free bonds from the crystal lattice leading to a reduction of these centres;
- **Field-effect passivation** - Insulator materials are known for their high density of fixed charges. Through the creation of an electric field induced by the high density of these negative charges present in the dielectric is possible to avoid the passage of minority carriers to the back contact.

Apart from the passivation effect, with the right choice of material for this layer, the optical reflectance of the rear contact might increase as well.[30]

1.2.4.2 Light management

The optical path is defined by the distance that light travels inside a medium. With the reduction of the CIGS layer in a solar cell, the optical path decreases accordingly, followed by a reduction of the amount of light absorbed. To increase the optical path and, therefore, increase the probability of photons being absorbed in the CIGS layer, some light management strategies are currently being studied. Rajan *et. al.* developed an antireflective coating (ARC) to use in CIGS solar cells, avoiding part of the parasitic absorption and increasing the efficiency by 5%.[31] T. Lopes *et. al.* was able to double the optical path of light in a UTFSC by implementing a metal as a reflective layer on top of the rear contact, thus increasing its performance.[32] S. Morawiec *et. al.* developed a back reflector for solar cells based on Ag nanoparticles. Through the modification of the physical properties of the nanoparticles, it is possible to change the energy by which they oscillate collectively (localized surface plasmon resonance). The light near the localized surface plasmon resonance (LSPR) can be scattered through the formation of a propagating far-field by the nanoparticles.[33]

The scope of this work is to develop a working lift-off process to fabricate a modified rear contact. This novel structure has the purpose of increasing the optical path in the absorber layer, thus enhancing the efficiency of CIGS TFSC. The metals for that structure were chosen based on their optical properties, namely the reflectance for infrared wavelengths, and ultimately on their availability at INL. Hence, four metals, Ta, Cu, Pd, Pt, are tested. The passivation effects are conducted through the use of a dielectric layer SiO_2.

2.1 Device optical simulations

The optical simulations were done using *Lumerical*, a powerful photonic simulation software that uses a Finite-Difference Time-Domain (FDTD) method to solve the Maxwell's equations, in all types of geometries and materials:

$$\frac{\partial \vec{\boldsymbol{D}}}{\partial t} = \nabla * \vec{\boldsymbol{H}} \tag{5}$$

$$\vec{\boldsymbol{D}}(\omega) = \varepsilon_0 \varepsilon_r(\omega) \vec{\boldsymbol{E}}(\omega) \tag{6}$$

$$\frac{\vec{d}\,\vec{\boldsymbol{H}}}{\partial t} = -\frac{1}{\mu_0} \nabla * \vec{\boldsymbol{E}} \tag{7}$$

where D, H, and E are the displacement, magnetic and electric fields, respectively.

The software has the ability to split the total volume of the simulation in smaller cells, creating a grid. The interactions between the electromagnetic waves with the material in each of the grid cells are then solved individually. Reducing the mesh size will lead to a more accurate representation of the behavior of light when in contact with the structure, nonetheless, that is followed by an increase in simulation time and required memory.

In our case, the structure that we wanted to simulate is formed by a standard stack of the several layers that compose a CIGS solar cell combined with our modified rear contact. Taking into account that our rear contact has a periodic pattern, with trenches every 2.8 µm, the simulation was defined for only one of these periods. Afterwards, the simulation boundaries were defined. For the upper and lower boundaries, we used a perfectly matched layer (PML). The sole purpose of this layer is to absorb all the incoming light, with the reflection being almost zero. For the side boundaries, we used symmetric and anti-symmetric layers, chosen according to the electric field polarization of the source. Through the use of these types of boundaries we were able to replicate the results for the rest of the simulation region, thus reducing the amount of memory needed for each simulation, translating into a decrease of the time needed. Regarding the mesh, we decided to set each individual cell with a volume of 5 nm^3. Our smaller feature was the $MoSe_2$ layer, with a thickness of 5 nm, hence the mesh size chosen seemed to be a reasonable value, providing a good trade-off between simulation accuracy and time spent.

2.2 Device fabrication

In this chapter, both fabrication and characterization of the devices will be covered. Furthermore, it is important to note that part of the fabrication is done by other groups. The first Mo deposition is made by the Uppsala University, in Sweden. The modification of the back contact is made in-house, by our group at INL. The remaining layers that compose the solar cell are deposited at Imec, in Belgium. A first electrical characterization is also made at Imec, with J-V and EQE measurements. These measurements are then repeated at INL, to ensure the fidelity of the results.

2.2.1 Rear contact structure

The cell fabrication process started at the Uppsala University where the Mo layer was deposited on top of a 5x5 cm^2 SLG substrate with 1 mm of thickness. The Mo layer was deposited in a vertical inline MRC 603 DC sputtering system with a pressure of 0.8 Pa and a power of 1500 W. The Mo target used has a purity of 99.995%, and the SLG substrates pass in front of it with a speed of 7 cm/min. The result is an evenly distributed Mo layer with a thickness of 350 nm. Afterwards, the samples were shipped to INL, where they went through a cleaning process. The cleaning process included three consecutive ultrasound baths in acetone (10 minutes), isopropanol (10 minutes) and water (5 minutes). The next step was the 40 nm metal deposition. The metals used (Pd, Pt, Ta, Cu) were deposited using a Kenosistec system, a multi-target DC sputtering equipment. Thereafter, a 25 nm dielectric deposition (SiO_2), at 300 ºC, was done using an SPTS PECVD system.

The optical lithographic step defines the patterning of the rear contact where the CIGS absorber comes in touch with the Mo layer. First, the samples go through a hexamethyldisilazane (HMDS) treatment for 15 minutes in a vapor prime oven. The objective is to enhance the adhesion of the photoresist that will be coated. Afterwards, a bilayer of photoresist (LOR (500 nm)/AZ1505 (600 nm)) was coated on top of the sample using a SUSS Microtec Gamma Cluster Track, an automated equipment that runs the coating and all the inherent steps (**figure 2.1**). The Mo/Ta/SiO_2 sample had problems during the photoresist coating, with different thicknesses throughout its surface, and after four reworks, it was impossible to continue with this sample.

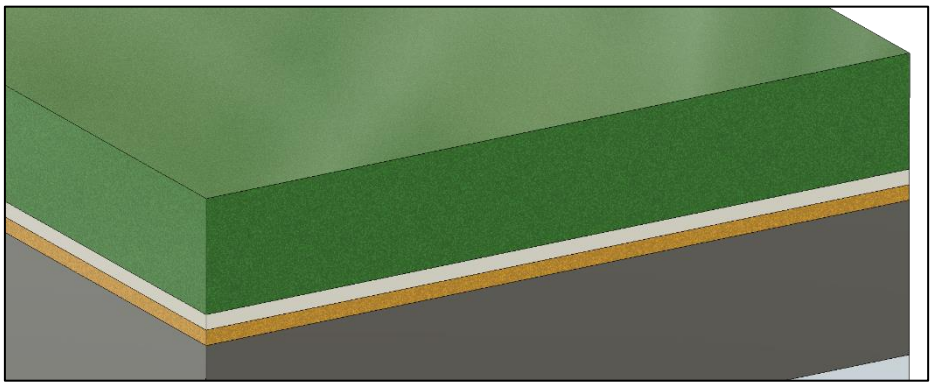

Figure 2.1 – a) SLG/Mo substrate after metal and dielectric depositions;
b) Substrate coating of the photoresist (LOR/AZ1505) stack.

The samples were exposed using direct-write laser lithography. The equipment, DWL2000, makes use of a 405 nm laser to expose the desired pattern into the photoresist. The mask used consisted of trenches with 900 nm of width and a pitch of 2.8 µm. These feature sizes were chosen based on the calibrations made, which are the scope of this work and are better described in **chapter 3**. For the exposure conditions, the focus setting was set on -10, while the laser intensity was set on 70%. It took about 20 minutes to expose the area of the pattern, and afterwards, the sample went back to the SUSS track to be developed. The development of both photoresists was done at the same time. The developer (AZ400K) was poured on top of the samples, thus creating a puddle of developer. After 45 seconds, the sample was spanned at high rotations while water was poured in order to clean it.

The next step was the reactive ion etching (RIE) of the metal and dielectric layers (**figure 2.2a** and **2.2b**), in order to open the trenches for the contact between Mo and CIGS. For that, an SPTS ICP system, based on chlorine ions, was used. This process took 75 seconds, in order to open the lines through the dielectric, the metal and a slight over etch of the Mo layer. After the etch, an optical inspection was made, where it was seen that the Cu sample had a re-deposition of copper.

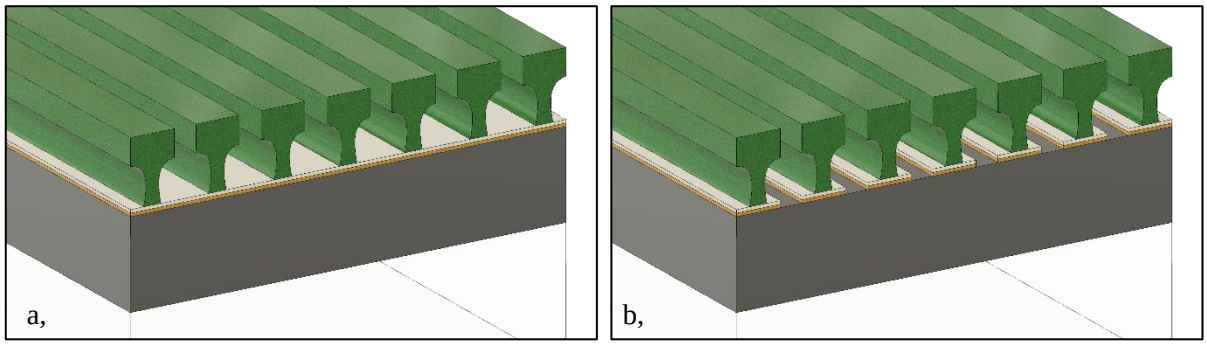

Figure 2.2 – a) Photoresist stack development; b) Sample after 75 seconds of etch, with trenches opened until the Mo layer.

Afterwards, the 100 nm deposition of the second Mo layer (also at INL), with the purpose to fill the trenches previously opened, thus preventing a metal diffusion during the CIGS growth, was done. The final step was the lift-off of the photoresist. The samples underwent an ultrasound bath at 60 ºC while submerged in mr-rem 500, a remover used for LOR photoresist. The lift-off was complete after approximately 10 minutes, thereafter the samples were submerged in isopropanol, for another 5 minutes, in order to clean them. The resulting structure can be seen in **figure 2.3**.

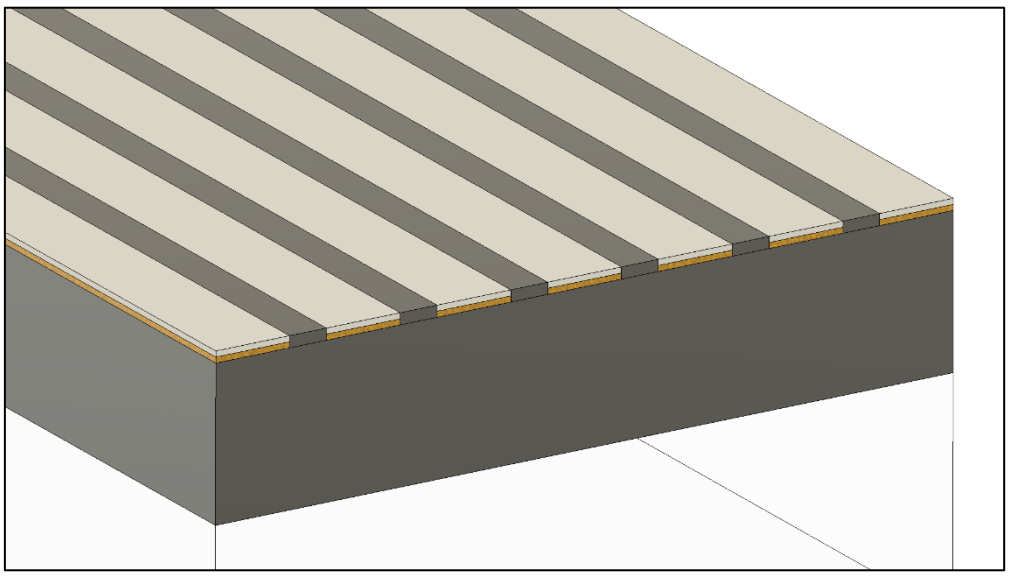

Figure 2.3 – Rear contact after the fabrication of the novel structure.

Prior to the shipping to Imec, the reference sample (Mo), the passivated (Mo/SiO_2) and the other two samples with metal ($Mo/Pd/SiO_2$ and $Mo/Pt/SiO_2$) underwent a thorough study using scanning electron microscopy (SEM), atomic force microscopy (AFM), and spectrophotometry. All the results will be addressed in **sections 3.3 and 3.4**.

2.2.2 Solar cell

The remaining layers were deposited at Imec as previously referred. The first layer to be deposited was a 7 nm NaF layer through thermal evaporation. The deposition took 4 minutes and 30 seconds with the crucible at 790 ºC. In our rear contact, the existence of a SiO_2 dielectric layer will hinder the Na diffusion from the SLG to the CIGS layer. For that reason and by knowing the importance of Na in CIGS solar cells performance (mentioned in **section 1.2.4**), a 7 nm NaF layer was added to the

process. Afterwards, a 500 nm deposition of CIGS was made using the co-evaporation method in a high vacuum chamber. It is important to mention that this deposition method did not produce a Ga grading, as seen in other studies. The CIGS was grown at a temperature of 550 ºC, while the crucibles Cu, Ga, In, Se where at 1338 ºC, 1080 ºC, 1050 ºC, and 249 ºC, respectively. The deposition took 9 minutes, after that, the Cu, Ga and In shutter were closed while the Se was left open for another 90 seconds. A more detailed description of this process can be found elsewhere[22]. The [Cu]/([In] + [Ga]) ratios vary between 0.79 and 0.91 while the [Ga]/([Ga]+[In]) ratios between 0.29-0.34. After the deposition step, the samples were left in the chamber to cool down. The 50 nm CdS layer was deposited using a standard chemical bath deposition process at 60 ºC for 5 minutes. The TCO stack, namely the i:ZnO (100 nm) and the Al:ZnO (400 nm), was sputtered. The grid of Ni/Ag/Ni was also sputtered with the help of a physical mask on top of the samples, in order to get the desired pattern. At this point, the completed solar cell had the appearance of the one in **figure 2. 4.**

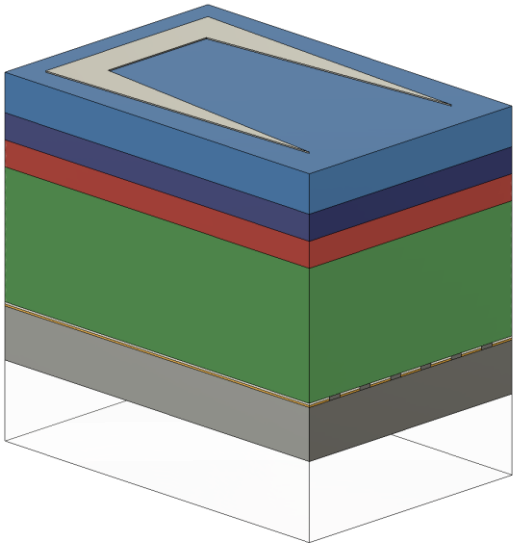

Figure 2.4 – CIGS solar cell after the deposition of the remaining layers on top of the rear structure.

2.3 Characterization techniques

The samples were characterized in two different phases. The first was after the modified rear contact fabrication, while the second was after the solar cell was completed.

For the SEM cross-sections of the samples a NovaNanoSEM650 system was used. The parameters used varied between samples and according to the materials that were being observed.

The morphology analysis was done using Atomic Force Microscopy (AFM) with an AFM Dimension Icon system. The measurement was made on tapping mode, with a scan rate of 1Hz.

Relative optical reflectance measurements were made with a UV-VIS NIR Spectrophotometer. The system possesses an integrating sphere allowing to measure both total and diffuse relative reflectance. These measurements were made from 300 to 1100 nm with a step of 10 nm.

The J-V measurements were made with an Oriel LSH-7320 ABA LED Solar Simulator system that uses a tungsten halogen lamp to simulate the solar spectrum (AM 1.5) and a Keithley 2420 Source Meter to apply a voltage between -0.5 V and 0.8 V with a step of 10 mV and read the correspondent current.

EQE measurements were done using a QEX10 system with a monochromatic probe light with a wavelength range between 300 and 1100 nm and a step of 10 nm.

In this chapter, the results obtained will be presented and discussed. First, a series of simulations to study the behavior of light inside a CIGS solar cell were made using *Lumerical*. At this point, the objective of these simulations was to prove that the novel structure at the rear contact, proposed to decrease the optical losses in CIGS solar fulfilled, in fact, its purpose. Thereafter, the results regarding every calibration for the processes needed to fabricate the rear contact will be shown. Then, a two-step characterization, using SEM, AFM, and spectrophotometry, prior and after the deposition of the remaining layers that are not fabricated at INL and compose the solar cell will be depicted. Finally, two alternative structures will be proposed.

3.1 Lumerical Simulations

In this section, we start by presenting the numerical model used by *Lumerical* in the optical simulations. Afterwards, all the simulations made will be presented. First, the simulations depicting the problems behind the thickness reduction of a CIGS solar cell, with a comparative study between CIGS solar cells with different thicknesses and their respective light absorption. Thereafter, simulations implementing a possible solution to increase the optical length and therefore increase the absorption inside CIGS ultrathin film solar cells will be presented.

All the structures simulated can be seen in **annex 6.1**. The author would like to emphasize that simulations present in this work only consider optical losses, thus no conclusions regarding electrical losses can be made, such as light scattering at grain boundaries, recombination, defects, pinholes, among others.

3.1.1 Numerical model – Finite-difference time-domain (FDTD)

The numerical model used by *Lumerical* to solve electromagnetic problems is the FDTD method. The software transforms the 3d simulation volume into a mesh and then simulates each one of the nodes, on that mesh, separately. The simulations are based on the complex refractive index (n,k) of the materials used. For Ta, Cu, Pd, and Pt these values were taken from [34]. For the CIGS, with [Ga/Ga+In)] = 0.30, the values were taken from [35].

First, the vector of the electric field is calculated for all the nodes of the mesh. Subsequently, through the integration of that electric field in each domain it is possible to calculate the respective power absorbed (P_{ABS}):

$$p_{ABS} = \frac{1}{2}\omega\varepsilon''|\boldsymbol{E}|^2 \tag{8}$$

where, ω, corresponds to the light angular frequency, ε´´, to the imaginary component of the dielectric permittivity and $|\boldsymbol{E}|^2$, to the electrical field intensity. P_{ABS} is then normalized by the source power in order to obtain the absorption per unit volume, p_{ABS}. Through the integration of p_{ABS}, at a certain wavelength (λ), is then possible to compute the total light absorption in a region:

$$Abs(\lambda) = \int p_{ABS}\ dV \tag{9}$$

It is important to note that, in CIGS solar cells, the great majority of the light that produces photogenerated current, is absorbed in the CIGS layer. Thus, in these simulations, p_{ABS} is only integrated in this layer, since light absorbed on other layers, will most probably lead to parasitic absorption.

Assuming that each absorbed photon in CIGS generates a carrier, the software is able to calculate J_{SC} in that layer. Consequently, through the integration of the absorption in the CIGS layer with the incident AM1.5 solar power spectrum, for the range of desired wavelengths, the J_{SC} is calculated:

$$J_{SC} = q \int \frac{\lambda}{hc} Abs(\lambda) I_{AM\ 1.5}(\lambda)\ d(\lambda) \tag{10}$$

where, q, represents the electronic charge, h, the Planck constant and c, the free space light speed. In the case of CIGS, the wavelength considered was from 300 nm to 1100 nm. Below 300 nm, the incident photons are absorbed by the front contact, the window layer, and the buffer layer, thus not contributing to the photogenerated current in the CIGS absorber. For wavelengths above 1100 nm, the energy of light is below the bandgap of the CIGS layer, making impossible for the photons to be absorbed there.

Finally, the author would like to make note that, after each simulation, a comparison between the FDTD result and the transfer matrix analytical formalism is performed. The precision is evaluated based on how much both plots overlap. All the simulations presented in this thesis, shown good precision.

3.1.2 Standard, thin-film, and ultrathin film CIGS solar cells

In this section, the simulation results that allow for a comparative study between conventional CIGS solar cells with different absorber thicknesses and their respective light absorption are shown.

In **figure 3.1a** and **figure 3.1b** are the simulated absorptance in the CIGS absorber and the simulated parasitic absorptance in the Mo rear contact, respectively. Additionally, the currents associated with each device are summarized in **table 1**.

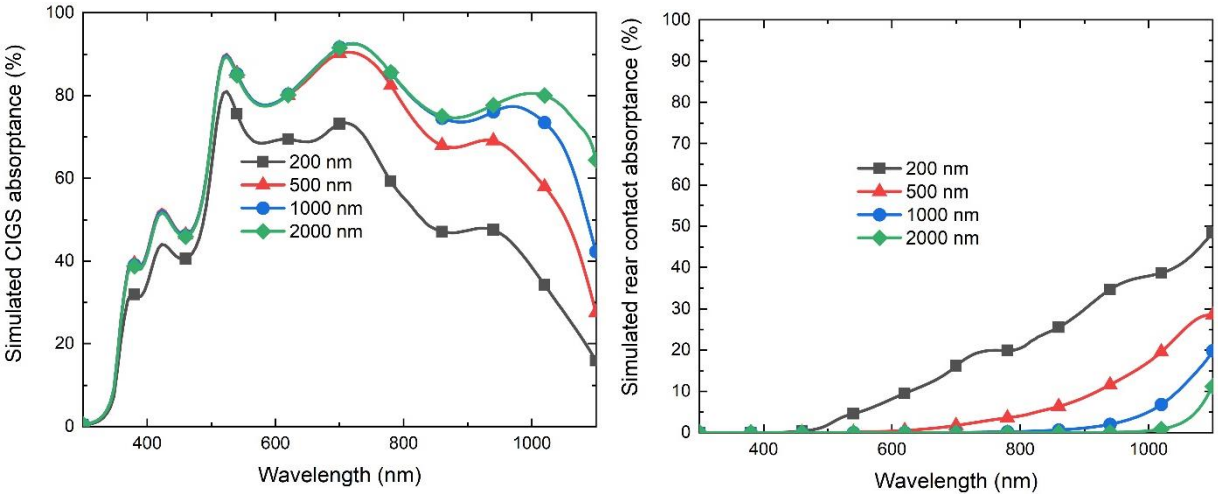

Figure 3.1 – a) Simulated CIGS absorptance for several thicknesses; b) Simulated Rear contact absorptance for the several thicknesses of CIGS.

As the thickness of the devices is decreased, the simulated results exhibit a reduction of the light absorbed by the CIGS layer whilst the respective parasitic absorption on the rear contact increases. All the cells have the same standard rear contact, however, for the cells with thinner absorbers, a considerable amount of light passes through the absorber, thus reaching the rear contact, translating in the increase of the parasitic absorption referred before. The calculated J_{SC} for the standard cell (2000 nm) is 33.14 mA/cm^2 and for the ultrathin is 30.62 mA/cm^2. Considering this, the optical losses when these two devices are compared is of 2.52 mA/cm^2. Moreover, and even though it is out of the scope of this work if the thickness is decreased even further (200 nm) an optical loss of 9.48 mA/cm^2 emerges when in comparison with the standard device, emphasizing the deficient absorption of the former. It is

also important to mention that the majority of the optical losses occur for near-infrared (NIR) wavelengths. The low energy photons with a low absorption coefficient combined with the reduced thickness of the absorber contribute to that occurrence[36].

Table 1 – Simulated J_{SC} and parasitic absorption for the CIGS solar cells with different thicknesses.

Device thickness	Simulated short circuit current J_{SC} (mA/cm^2)	Parasitic absorption at the rear J_{SC} losses (mA/cm^2)
200 nm	23.66	7.92
500 nm	30.62	2.50
1000 nm	32.44	0.76
2000 nm	33.14	0.18

The achieved simulated results for the standard (2000 nm) CIGS solar cell regarding the J_{SC} are not in accordance with the current state of the art fabricated devices with the same thicknesses. For that reason it is also important to note that the simulations made in this work use a CIGS absorber layer that is relatively simple, while, for example, the current world-record CIGS solar cell (22.9%), published in an article, with a J_{SC} of 38.5 mA/cm^2, has a highly engineered absorber layer and, at the same time, an antireflective coating[37].

As seen above, with the simulations proving that a significant amount of light results in parasitic absorption on the rear contact, and taking into account other works, where is shown that Mo plays a major role for this to occur due to its poor reflectivity[3, 4], a good solution may reside in the use of a high reflective metal on top of the rear contact, thus leading to an increase of the optical path.

3.1.3 Light management strategy to increase reflection at the rear contact

In the previous section, it was shown the impact that the reduction of the absorber thickness has in CIGS solar cells, mainly due to parasitic absorption on the rear contact. Here, simulations using an ultrathin film CIGS (500nm), combined with a 40 nm metallic layer on top of the rear contact will be performed. Taking into consideration that the final structure will have a SiO2 layer it was decided to include it in these simulations as well, for realism purposes. The simulation results can be seen in **figure 3.2**, while the Jsc calculated are represented in **table 2**.

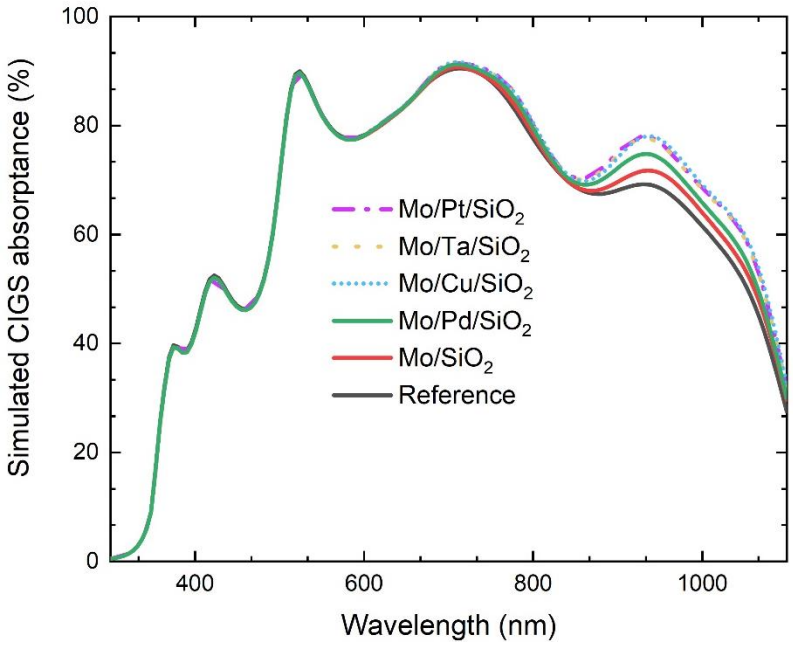

Figure 3.2 – Simulated CIGS absorptance for several metals used in the rear contact structure.

All the different metals gave rise to an enhancement on the CIGS absorption when in comparison with the ultrathin reference. The best result was achieved by the Mo/Cu/SiO_2 cell, with a J_{SC} improvement of 1.06 mA/cm^2 and a reduction of the parasitic absorption of 1.54 mA/cm^2, relatively to the reference cell. The Mo/Pt/SiO_2 cell gave similar results with an increase in the J_{SC} of 1.03 mA/cm^2 and a difference in the parasitic absorption of 1.57 mA/cm^2. Another relevant fact is that only by the incorporation of the SiO_2 insulator layer, an increase in the light absorption in CIGS is observed, thus revealing that the rear contact reflectance was increased.

Table 2 – Simulated J_{SC} and parasitic absorption for the CIGS solar cells with different metals.

Samples	Simulated short circuit current J_{SC} (mA/cm^2)	Parasitic absorption at the rear J_{SC} losses (mA/cm^2)
Mo/Cu/SiO_2	31.68	0.96
Mo/Pd/SiO_2	31.23	1.62
Mo/Pt/SiO_2	31.65	0.93
Mo/Ta/SiO_2	31.16	1.01
Mo/SiO_2	30.89	2.09
Reference	30.62	2.50

In all the cells with the metal in the rear contact, the enhancement in the CIGS absorption was smaller when in comparison with the decrease in parasitic absorption, giving another significant insight. In **figure 3.3**, the simulation results regarding the cells' total reflectance were depicted, showing evidence of an increase in reflection, for wavelengths above 800 nm, when the metal is added to the rear contact relatively to the reference cell. These results showed that although the metal layer represented an improvement on ultrathin film CIGS solar cells, by increasing the optical path, similar approaches are needed for the front contact, in order to avoid the light to escape through the top after being reflected.

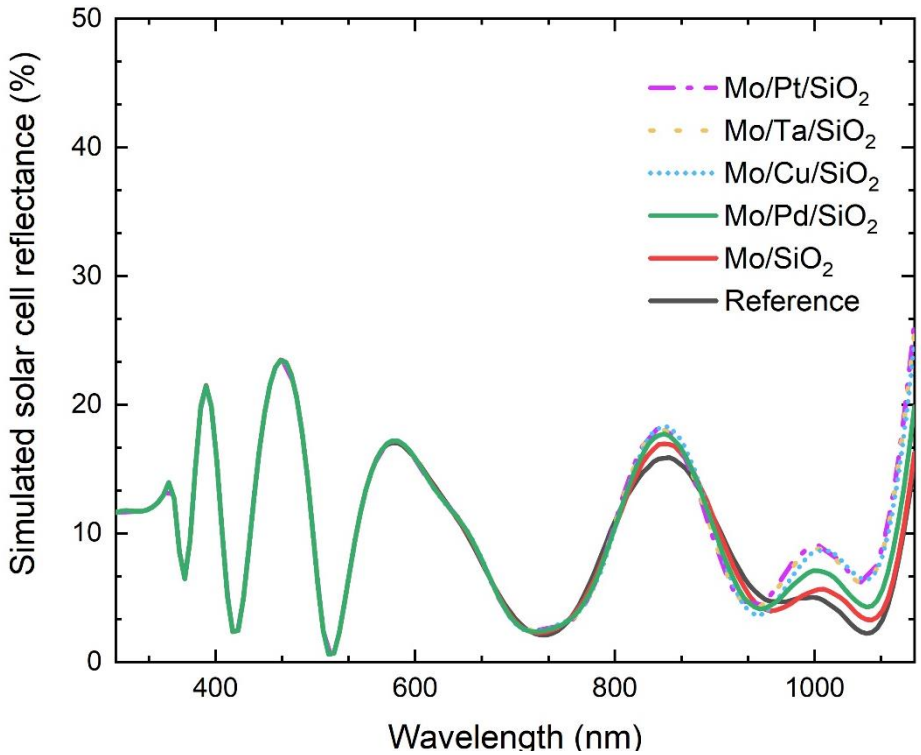

Figure 3.3 – Simulated solar cell reflectance for each metal used in the rear structure.

3.2 Calibrations

Nanofabrication tools inside the INL cleanroom are optimized to handle 8-inch wafers and to fabricate structures bigger than 2 microns. Considering that the structures we fabricate are smaller than that, with some features below 1 micron, it is important that all the tools used are recalibrated to handle these conditions.

3.2.1 Exposure conditions (Focus and Intensity) – Direct write Lithography

It is known that exposure dose and focus are two of the most important adjustable parameters that have an impact on the final trench width.[40] To make sure that the masks designed translated onto features with the critical sizes after the development, a calibration of the DWL laser beam was required. The mask designed for this purpose had trenches with 800 nanometers and a pitch of 2.5 microns (**figure 3.4**). The software used by DWL allows the repetition of the mask in several fields throughout the sample (2.5x2.5 cm). By exposing each field with different values of focus (focal position regarding the substrate), from -10 to 10, and intensity of the laser, from 60% to 100%, it is possible to see which value for each parameter will give us the most accurate feature sizes (*Focus-Exposure Matrix*).

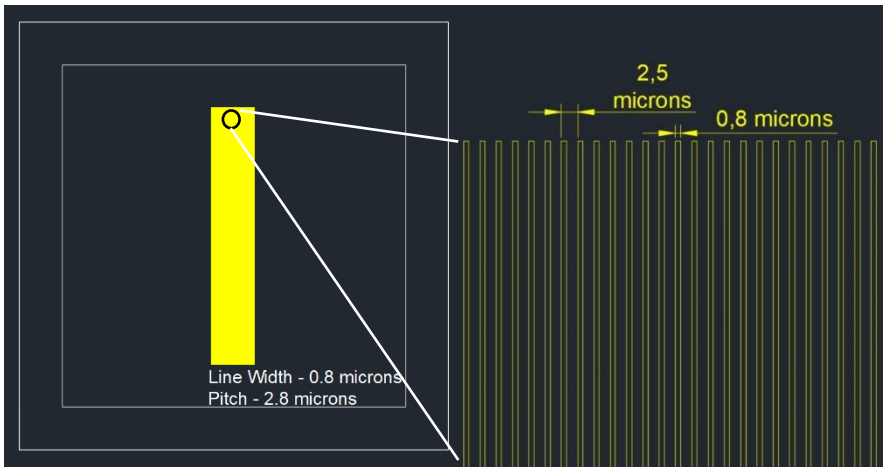

Figure 3.4 – Auto-CAD mask used in DWL for the laser calibration.

The results shown in **table 3** were obtained through optical inspection of each field, making four measurements of the trenches' width per image.

Table 3 – Exposure conditions vs Lines' width

Focus	Intensity (%)	1	2	3	4	Average
		Trenches width (µm)				
-10	60	0.88	0.82	0.84	0.8	0.84
	70	0.96	0.98	0.93	0.85	0.93
	80	1.09	1.08	0.98	1.02	1.04
	90	0.98	1.04	1.03	1.02	1.02
	100	1.04	1.11	0.99	1.02	1.04
0	60/70/80	Bad development				
	90	1.16	0.96	1.13	1.12	1.09
	100	1.23	1.14	1.04	1.03	1.11
10	60/70	Bad development				
	80	1.02	1.00	0.92	0.88	0.96
	90	1.05	1.10	1.03	1.02	1.05
	100	1.11	1.16	1.10	1.10	1.12

First of all, it is important to mention, that by the time this calibration was made the optimized conditions (calculated by the cleanroom engineers at INL, for their processes) were -10 and 60%, for the focus and intensity, respectively.

The calibration done gave consistent results with the literature, exhibiting an increase in the width of the lines as the exposure dose, represented by the intensity, was increased.[41] Regarding the focus, it was seen that the further away from the optimized value and for smaller intensities, the development was not properly done. For that reason, no measurements were made in those fields. On the other side, for higher intensities, the focus shows little or no variation on the feature sizes.

With these results, taking into account that we were near the machine physical limitations and that for higher intensities (from 70% to 100%) the feature sizes start to be more reproducible, it was decided to sacrifice part of the dimensions in order to have a more reproductive process. For that reason, the intended trenches width was changed to 900nm, allowing our process to follow the DWL regular calibrations, and therefore making all the other variables more controllable.

3.2.2 Photoresist development (LOR 5B) – Resist undercut

In this section, considering that the undercut of the LOR 5B photoresist plays a major role in the lift-off process[42], the objective was to understand the effect that the development time and the feature sizes (trenches width and pitch) had on the undercut produced.

An initial trial, using the development time calibrated for INL standard processes (60 seconds) was performed in a sample with a pitch variation between 1.8 and 3 microns. The results for the fields with a small and larger pitch can be seen in **figure 3.5**.

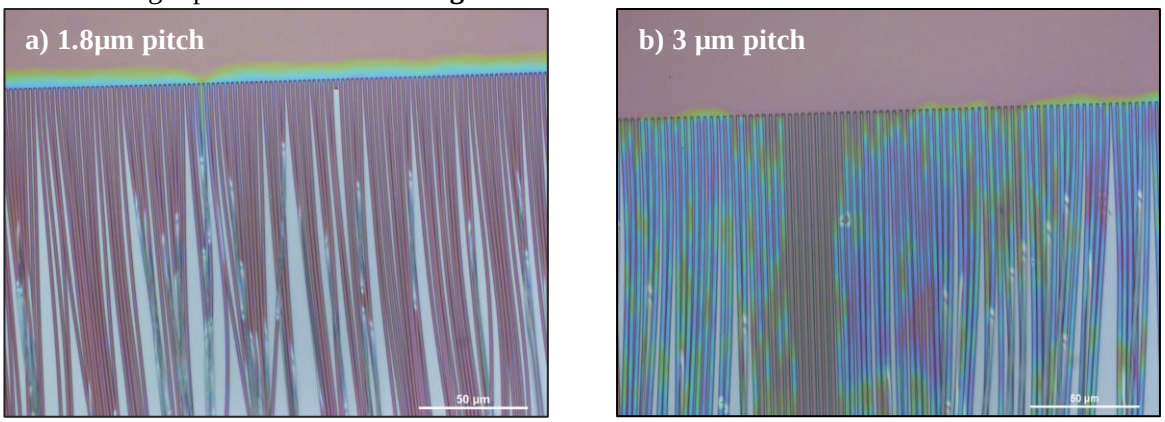

Figure 3.5 – Optical microscope images of the LOR photoresist undercut test for a) 1.8 µm pitch and b) 3 µm pitch, with 60 seconds of development.

The development time of 60 seconds for this first test lead to the immediate peel off of the photoresist (even for the field with 3 microns of pitch), meaning that its dissolution rate was higher than initially thought. Thereafter, a more elaborate experiment composed of 2 samples (45D, 30D) with different development times (45 and 30 seconds) was designed. The mask (**figure 3.6)** had 3 different areas with different purposes: in the first (left), 5 fields with a pitch variation, in the second (center), 4 fields with a line width variation, and the third (right), had features with 20 microns spaced 50 microns solely for control purposes.

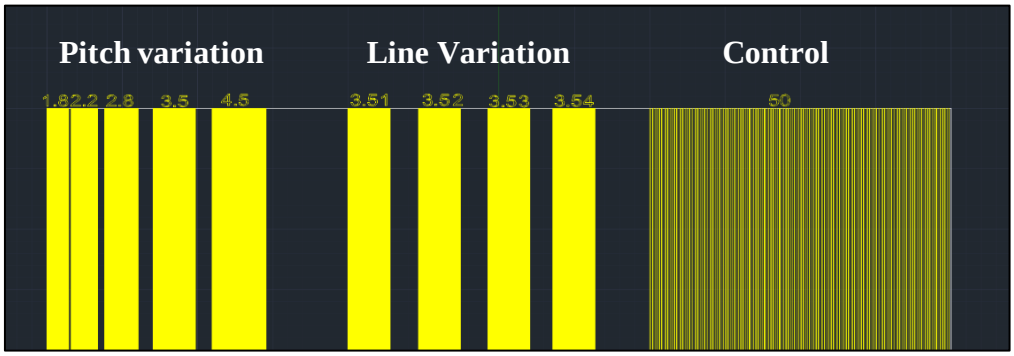

Figure 3.6 – Auto-CAD mask used for the calibration of the LOR photoresist undercut.

In **figure 3.7**, it is possible to see the control fields for both development times. Moreover, in **figure 3.7b**, the evidence of an undercut profile can be observed alongside the feature and it is based on observations made by another group, using an optical microscope[43].

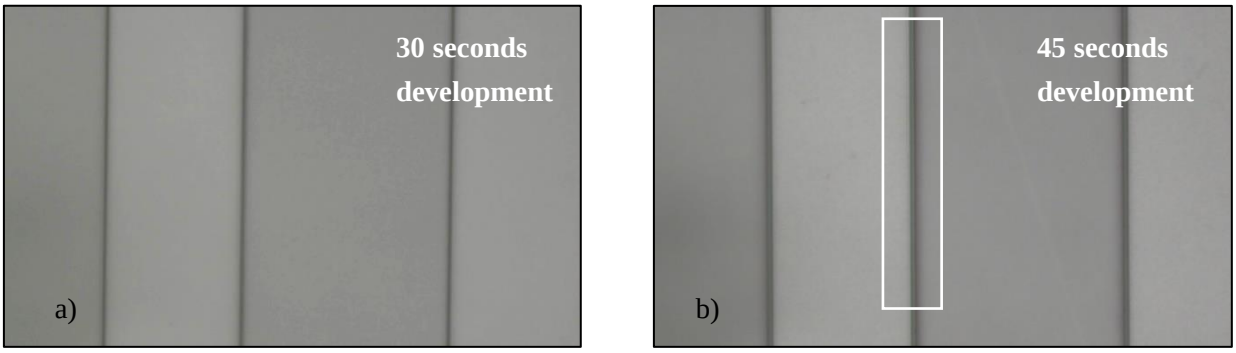

Figure 3.7 – Optical microscope images of the control fields for the undercut calibrations with a) 30 and 45 b) seconds development.

It is important to make note that, this time, none of the fields developed peeled off, proving that the undercut produced was less than 900nm, half of the smallest pitch, for both samples. Nonetheless, it was also important to have a more thorough study of the undercut produced. Bearing that in mind, some SEM images of the sample's cross-section were taken. From that analysis it was possible to draw two early conclusions: **i,** the pitch had a little influence in the undercut profile while the area of the samples with the variation of the line's width presented a significant change; **ii,** there was a major difference between 30 (**figure 3.8**) and 45 seconds (**figure 3.9**) of development, since the former does not represent enough time to fully open the trenches in all the fields and, at the same time, produce a proper undercut (defined by the white circle **in figure 3.9d**).

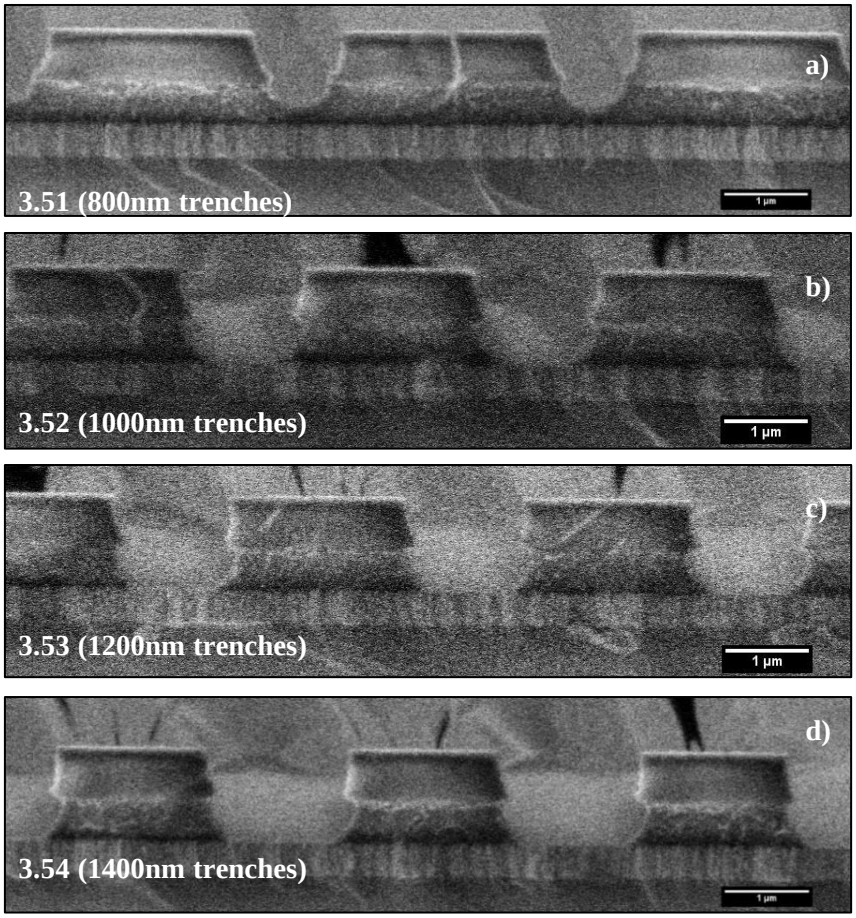

Figure 3.8 – Undercut profile after 30 seconds of development for trenches with a) 800, b) 1000, c)1200 and d) 1400 nm.

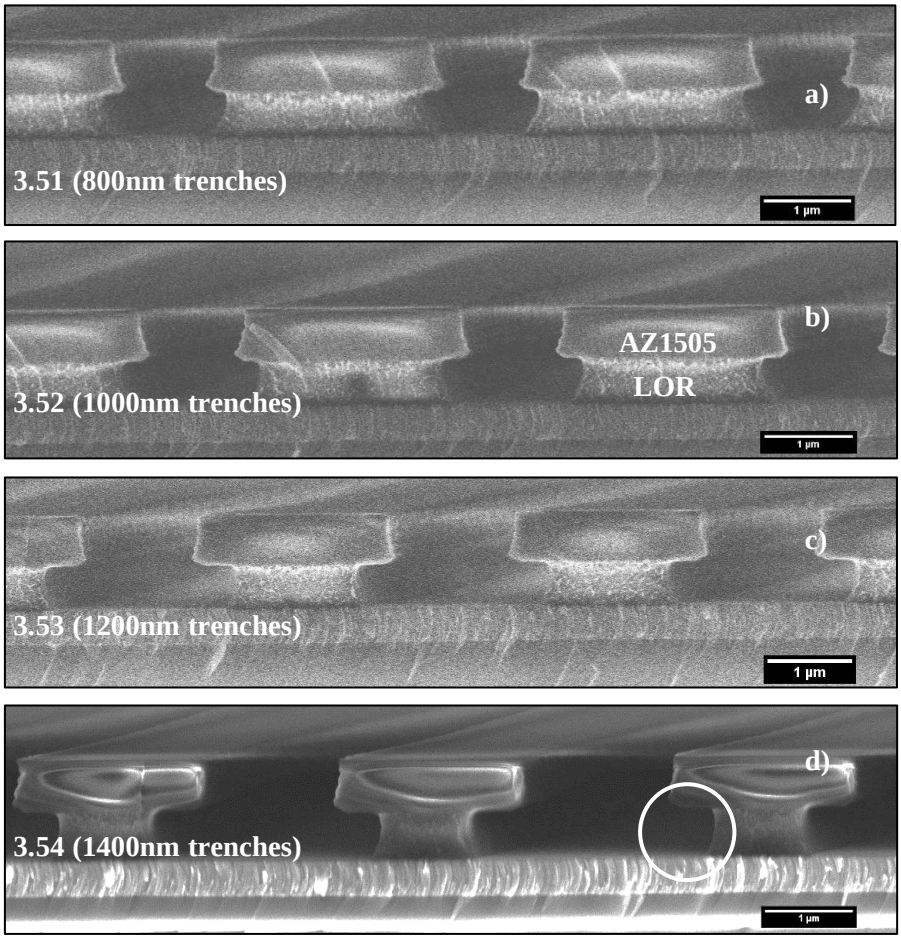

Figure 3.9 - Undercut profile after 45 seconds of development for trenches with a) 800, b) 1000, c)1200 and d) 1400 nm.

In sample 45D, it was possible to verify that, in contrast to sample 30D, the lines were fully developed, and an undercut was produced. These findings are in accordance with preliminary results found through the images in **figure 3.7**. Furthermore, it was possible to observe the appearance of a pattern: as the line's width increased, the size of the undercut increased accordingly. Through **table 4**, containing all the measurements made using the images in **figure 3.8 and figure 3.9**, the pattern became even more evident. Seven measurements per image were made. The first two regarding the line's width, the third, regarding the pitch, and the last four, the undercut. Further explanation about how the measurements were taken can be found in **annex 6.2.**

Table 4 – Undercut measurements in sample 45D

Fields (trench width (µm))	Trench width (µm)		Pitch (µm)	Undercut size (µm)				
	1	2	3	4	5	6	7	Average
3.51 (0.80)	0.90	0.90	3.60	0.20	0.18	0.18	0.16	0.18
3.52 (1.00)	1.00	1.00	3.70	0.32	0.25	0.27	0.28	0.28
3.53 (1.20)	1.20	1.30	3.70	0.48	0.38	0.38	0.36	0.40
3.54 (1.40)	1.50	1.60	3.70	0.44	0.47	0.47	0.48	0.47

The first thing that needs to be addressed is that the measurements made were not completely precise since the sample was slightly tilted inside the SEM. Several studies show that when observing a sample with an insulator on top using an SEM, artifacts may appear due to a phenomenon called charging effect, where the accumulation of static charges influences negatively the final image.[5,6]

A known solution for this problem is to apply lower energies and currents or, as in our case, by tilting the sample.[46] Nevertheless, and despite the efforts made, this phenomenon is visible in **figure 3.8**, throughout the fields.

As referred above, the results obtained show a clear pattern, with an almost linear increase of the undercut, from 180 nm to 500 nm, as the line´s width was increased, from 800 nm to 1400 nm. Furthermore, according to the datasheet of LOR 5B photoresist[47], the minimum reproducible undercut was 500 nm. Our findings prove that is possible to not only produce a smaller undercut but also control it under the supposed minimum limit.

In section 2.1, it was confirmed that 900 nm was a reasonable width for the lines, considering the limitations of the DWL. In this section, it was possible to verify that for a width of 900 nm it was expected to get an undercut between 200 to 300 nm. Taking into account these promising results, it was decided to maintain the 900 nm for future calibration steps.

3.2.3 Metal and insulator etch (RIE) – Effects on the photoresist

Here, the objective was to verify if 45 seconds of etching had a negative influence on the photoresist that could lead to a problem during lift-off. Considering that the photoresist acts as a sacrificial layer, it was necessary to guarantee that the photoresist size and thickness would be maintained to a minimum. For that reason, measurements were made to a sample after the etch step (**figure 3.10**).

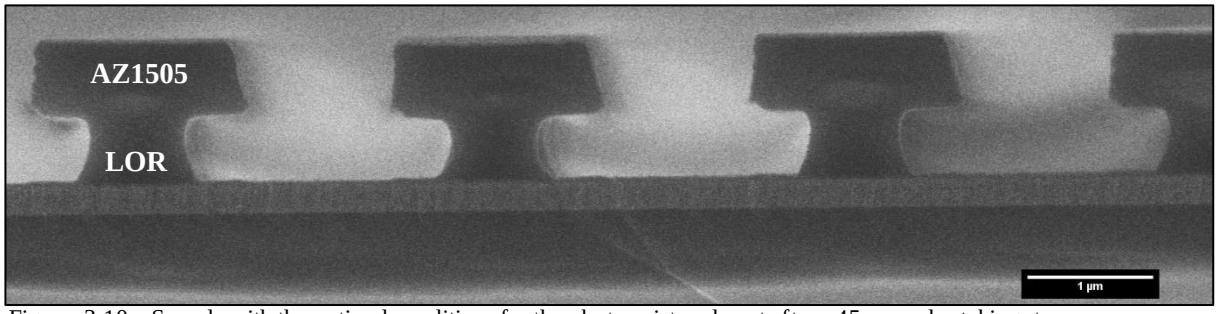

Figure 3.10 – Sample with the optimal conditions for the photoresist undercut after a 45 seconds etching step.

The results showed an increase in the trenches width, from 900 nm to about 1000 nm, meaning that, consequently, the contact area will increase in 100 nm. Nonetheless, that loss in the effective reflection area was not expected to be significant since there will be 1800 nm between contacts. That means that the active area, where it is supposed to exist an increase in reflection, is of 64%. Additionally, it was also found an increase in the LOR undercut, but since it was observed that the structural integrity of the photoresist was maintained no concerns were taken into consideration.

3.2.4 Lift-off Tests

The lift-off tests were conducted to make sure that the desired metal lines could be properly patterned using this process. Two tests were carried, one with 10 nm of copper and another with 60 nm. The images taken can be seen in **figure 3.11**.

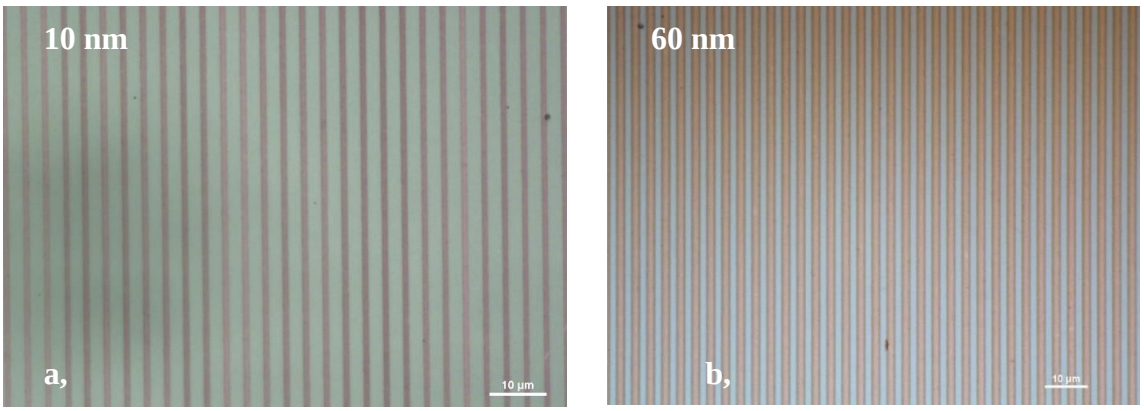

Figure 3.11 – Samples with a) 10 nm and b) 60 nm of copper after lift-off.

According to the literature, specific photoresists for lift-off (such as LOR) can be used to remove layers of metal up to the same thickness as their own[48]. Considering that the layer of metal that we wanted to lift-off had a thickness of about 1/5 of the photoresist, our only concern was related to the formation of sidewalls, detected in previous tests with other photoresists (not shown in this work). Nonetheless, that was not observed in this study, with the lines of copper exhibiting a good resolution.

3.3 Substrate characterization

The characterization of the substrates, with a novel structure as rear contact, is shown in this section. The structure consists of a 40 nm layer of metal (Pd, Pt, Ta, Cu) between the Mo rear contact and a layer of SiO_2, 20nm, followed by a pattern with trenches of 900 nm and a pitch of 2.8 µm, made with a lithographic step. Afterwards, a second deposition of Mo is made inside the trenches previously opened, thus enabling the electrical contact between Mo and the CIGS layer.

Unfortunately, both samples with $Mo/Ta/SiO_2$ and $Mo/Cu/SiO_2$ did not survive the fabrication. The one with the Ta, had problems during the coating of the photoresist, with the LOR not being properly coated throughout the sample. The posterior removal using an O_2 plasma asher process lead to the burn of the photoresist. The sample with the Cu metal layer had problems during the etch step, with the redeposition of Cu by-products outside the trenches. Some studies report that in order to make these Cu originated compounds volatile, a temperature above 200 ºC was needed[9,10]. The equipment that we used at INL for the etch step is not calibrated for Cu and the process used is not temperature controlled. Moreover, if a temperature of 200 ºC was used, that would burn the photoresist, thus compromising the lift-off step. Notwithstanding, it was decided to proceed with the plan for the remaining three samples: Mo/SiO_2, $Mo/Pd/SiO_2$, and $Mo/Pt/SiO_2$.

3.3.1 Scan Electron Microscopy

After the fabrication was done, the samples were analyzed using the SEM in order to observe if the pattern obtained was in accordance with the intended. The images taken can be seen in **figure 3.12**.

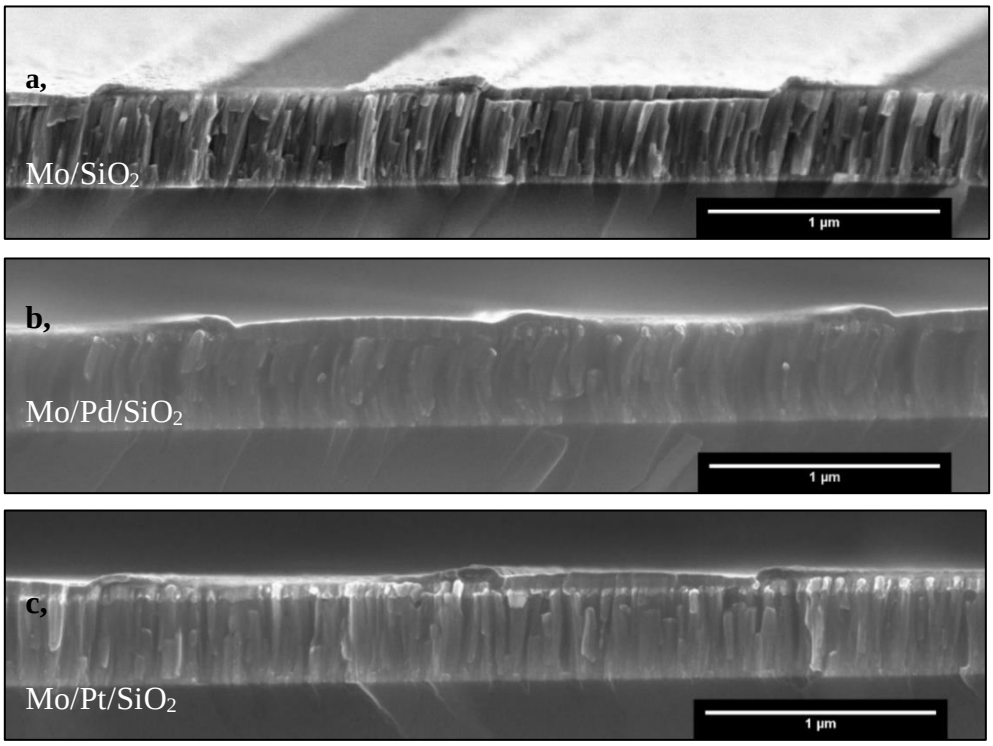

Figure 3.12 – SEM cross-section images of the rear contact samples fabricated: a) Mo/SiO2, b) Mo/Pd/SiO2 and c) Mo/Pt/SiO2.

Through the cross-section images, several problems were found. The first and more evident was the formation of sidewalls followed by a Mo residual deposition with approximately 200 nm alongside the trenches and throughout the sample. These problems are associated with the different levels of anisotropy between the processes used to fabricate the samples. As said above, the etch step was performed using RIE, which is a highly anisotropic process[51]. On the other side, the Mo deposition, through sputtering, although being also anisotropic, can range to a certain degree, depending on the characteristics of the machine used.

In **figure 3.13** it is possible to see that the etch created highly vertical trenches. Nonetheless, the deposition of Mo was not limited to the trench (white circles), with part being deposited under the LOR photoresist cavity previously created to help the lift-off. This excessive Mo deposition anticipates problems with the solar cell overall performance, considering that the Mo contact will increase substantially, followed by a reduction of the effective area with the dielectric/metal stack, what will probably lead to an increase in the parasitic absorption at the rear.

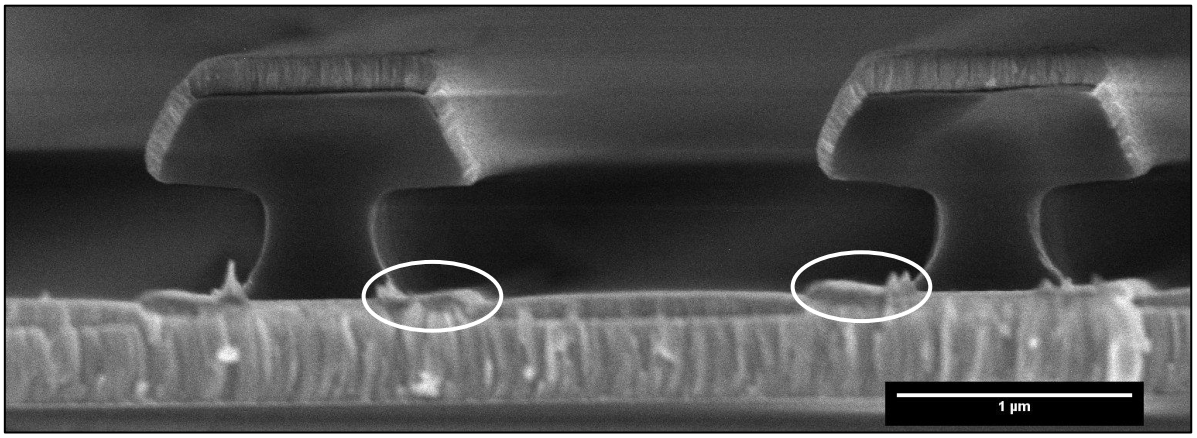

Figure 3.13 – SEM cross-section of a sample before lift-off to better understand the Mo deposition inside the trenches.

Another problem was found on sample Mo/Pt/SiO_2 (**figure 3.12c**), where the etch inside the trench was not complete, leaving a thin layer of Pt. After performing measurements to the cross-section, it was seen that the real thickness of the Pt layer, after its deposition, was 80 nm, meaning that the sputtering equipment was not correctly calibrated.

3.3.2 Atomic Force Microscopy

The morphology evaluation of the samples is crucial, in order to ensure that the sidewalls were not high enough to create problems during the deposition of the CIGS absorber layer. The profile measurements of the samples can be found in **annex 6.3**. It was also possible to verify the sample uniformity using the AFM, as seen through **figure 3.14**.

From the profiles obtained through the profile images, it was calculated that the average sidewalls' height was 56 nm, 66 nm, and 65 nm, for Mo/SiO_2, Mo/Pd/SiO_2, and Mo/Pt/SiO_2, respectively. CIGS is a complex material, with deposition methods not as straightforward as one might think. Negami *et. al.* [52] showed that a reduction of the CIGS thickness to 500 nm could lead to an increase in shunt conductance, only due to the fact that the roughness of the film was in the same order of the film thickness itself. Taking this into account, one might consider that even 50 nm sidewalls can negatively influence the deposition of the 500 nm CIGS thin film, affecting its morphology, thus creating pinholes that can lead to shunting pathways, and eventually can contribute to an overall loss in performance. Additionally, part of the purpose of the novel rear contact is to reduce the area of contact between Mo and CIGS, thus reducing the contact resistance. Through the profiles obtained with AFM, what we found, was that the difference of the contact area (Mo/CIGS) between samples (reference and the other) was only minor.

With regards to the general uniformity of the sample, the AFM analysis showed that the lift-off was consistent, even between samples, since all exhibit the same pattern and no residual remains were found in-between the trenches. It is important to realize that the sidewalls created do not represent a

defect on the lift-off step, but an issue with the isotropic Mo deposition. Moreover, the increase in the surface covered by Mo gave rise to another problem. It was found that the active area for the Mo/SiO_2, $Mo/Pd/SiO_2$, and $Mo/Pt/SiO_2$ was of approximately 31, 28 and 29%, respectively. These results proved to be far from great, since they will most likely translate into a decrease of the reflected light, thus reducing the overall solar cell performance.

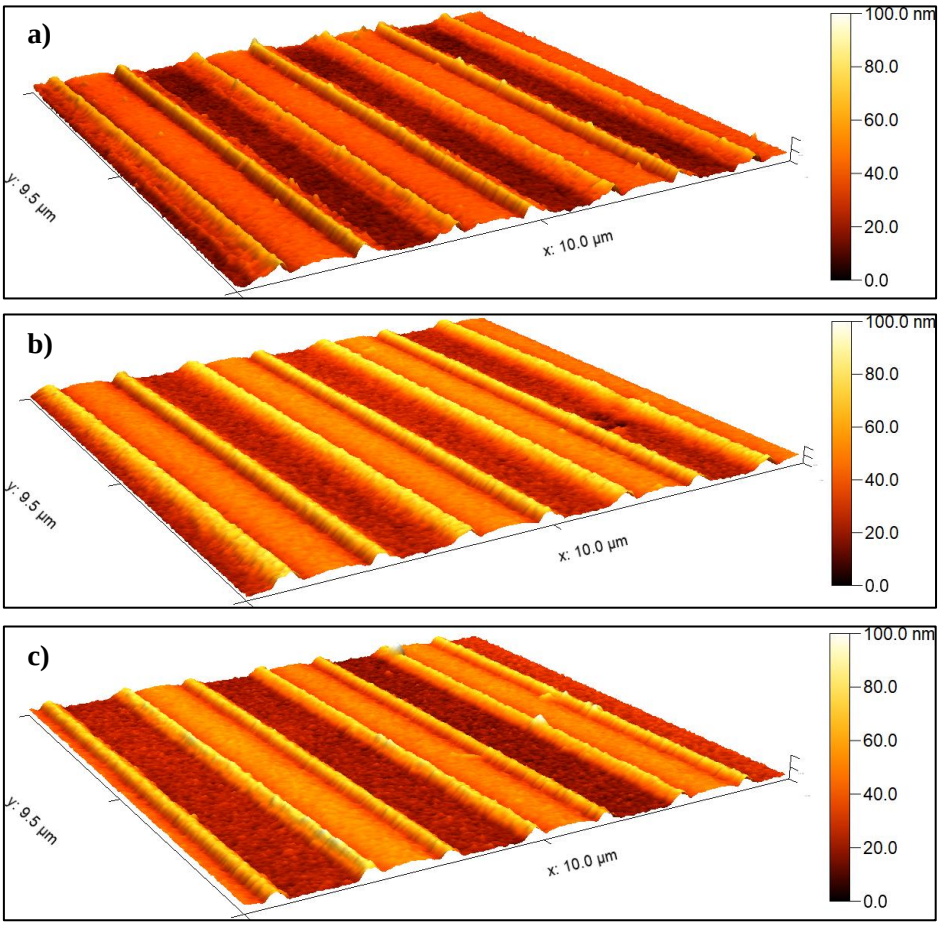

Figure 3.14 – AFM analysis of the rear contact samples fabricated: a) Mo/SiO2, b) Mo/Pd/SiO2 and c) Mo/Pt/SiO2.

3.3.3 Spectrophotometry

Since the purpose of this thesis was to develop a working fabrication process for the implementation of a metal at the rear contact of a CIGS solar cell, with the objective of increasing the reflectance, it was important to perform spectrophotometry measurements in the substrates produced. Both total and diffuse reflection were measured and can be seen in **figure 3.15**.

In **figure 3.15a** it is possible to confirm that the reference substrate exhibited a higher total relative reflectance throughout the entire interval of wavelengths. The reference substrate only had the Mo rear contact deposited on top, having a much more planar surface than the other three substrates. Therefore, it was expected that the specular reflectance heavily contributed to the total reflectance of the first. In contrast, the three substrates that underwent the processing steps to increase their reflection shown an increase of their diffuse relative reflectance, when compared with the reference substrate (**figure 3.15b)**. That increase in diffuse reflectance is probably associated with the patterned sidewalls alongside the contacts and throughout the substrate, making a texturization of the surface, characteristic that is known to increase the diffuse reflection[53]. The fact that the reference substrate exhibited a diffuse reflection near zero also supports this explanation. Additionally, it is proven that the diffuse reflection is more advantageous than specular since it scatters light[54]. For that reason, the problems found during the fabrication might, in fact, be beneficial for the performance of the solar cells.

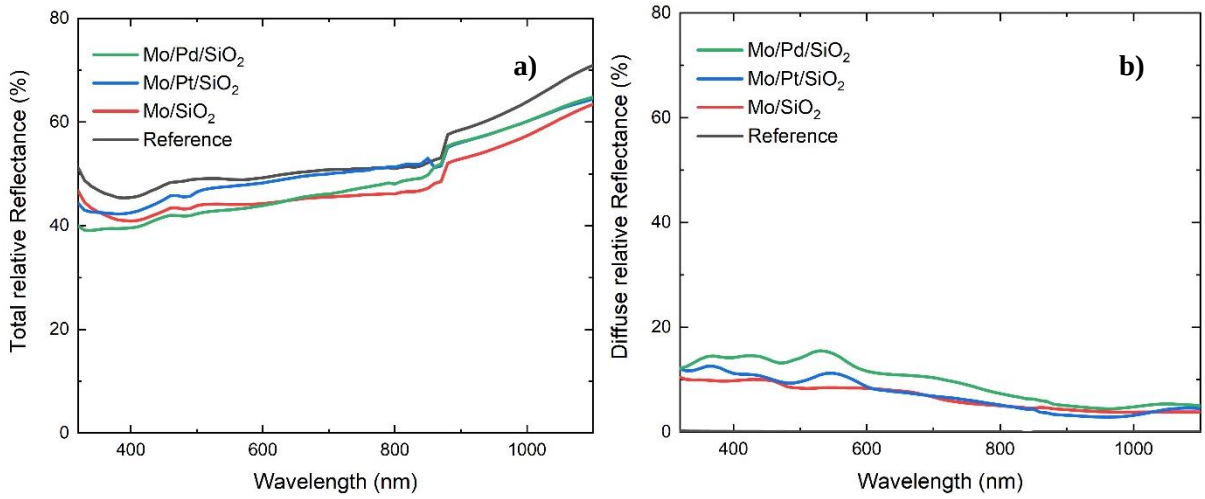

Figure 3.15 – a) Total relative reflectance and b) diffuse relative reflectance of the rear contact samples fabricated.

3.4 Solar cells characterization

As said in **chapter 2**, the substrates were sent to Imec, in Belgium, to deposit the remaining layers that compose the solar cell. After that, it was essential to do the inherent characterization to understand if the process developed brought some enhancements to their performance, thus always remembering that the fabrication process was not yet fully functional.

3.4.1 Spectrophotometry

The total relative reflectance of the fabricated solar cells is depicted in **figure 3.16**.

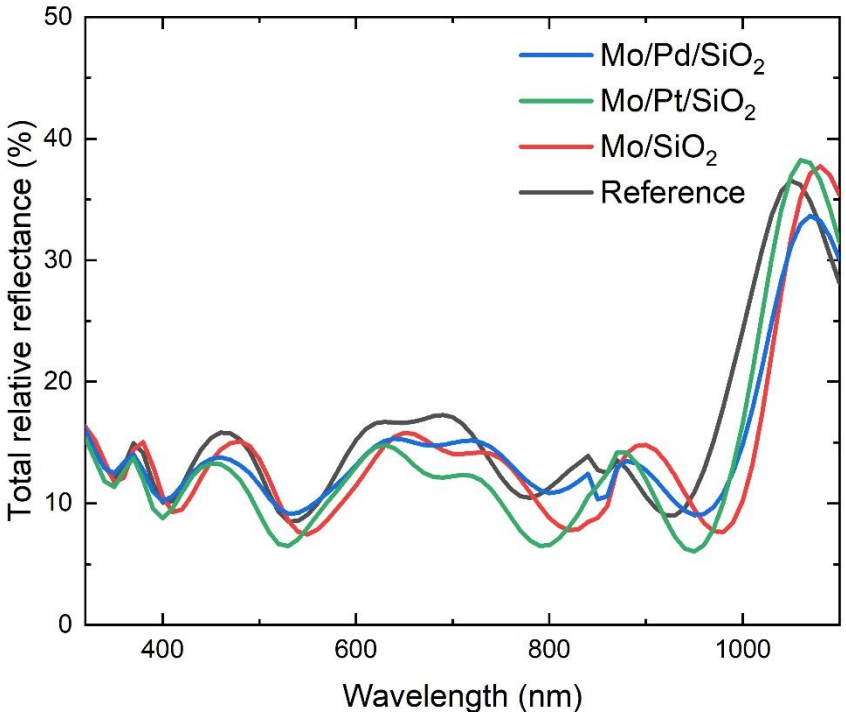

Figure 3.16 – Total relative reflectance of the solar cells fabricated.

From **figure 3.16** it was possible to verify that the reference cell had higher total relative reflectance across the majority of the spectrum. These results were in accordance with the characterization made to the samples prior to the deposition of the remaining layers. The spectral region (from 1050 to 1100 nm) where all the other samples showed an improvement when compared with the reference, could be explained by the reflection of light in the rear contact, even though the active area of reflection was severely reduced during the fabrication, as shown in **section 3.3.1** and **3.3.2**.

3.4.2 Electrical characterization

J-V and EQE measurements were performed in the solar cells. The representative illuminated J-V curves are shown in **figure 3.17**, whilst the EQE is depicted in **figure 3.18**. In **table 5**, all the summarized information regarding the figures of merit extracted from the J-V curves, the calculated J_{SC} from the EQE curves, and their respective standard deviation were shown. The J_{SC} calculations based on the EQE curves were extracted using the following equation[55]:

$$J_{SC} = q \int \phi(\lambda) EQE(\lambda)\, d(\lambda) \tag{11}$$

where, q, represents the electron charge, and, ϕ, the photon flux.

A first analysis of the illuminated J-V curves (**figure 3.17**) allowed us to observe steep slopes in the first and third quadrant, for all four solar cells. These are obvious signs of high series and low shunt resistance[56]. Moreover, when comparing the reference with the three other cells, it could be seen that the first presented a higher shunt resistance (defined by the slopes of the curves in the third quadrant). The CIGS growth has probably a role in this behavior, since its deposition on top of the sidewalls, present on all samples with exception of the reference, could lead to the formation of a higher number of pinholes, thus increasing the amount of shunts. In contrast, as expected, the reference presented a higher contact resistance, due to the fact that the area of the Mo contact was slightly higher for that sample.

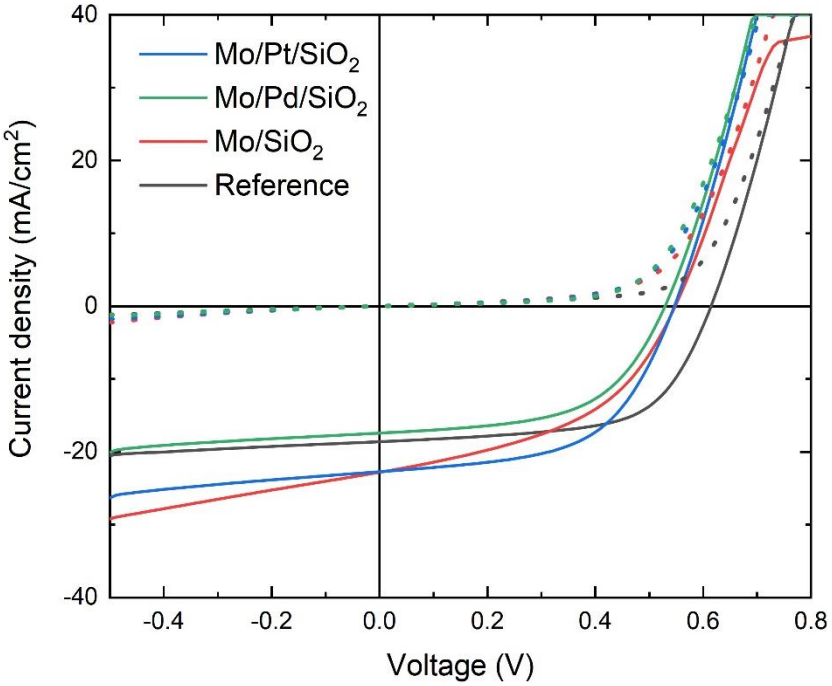

Figure 3.17 – Illuminated and Dark (dotted lines) J-V curves of the solar cells fabricated.

Another evidence of the presence of shunt paths is the difference between the J_{SC} taken from the J-V curves and the one calculated from the EQE (**table 5**), with the first considerably higher than the latter. During the EQE measurements, the cell is irradiated only in a fraction of its area making the non-illuminated area act as a shunting load. If the total shunt resistance is higher than in the representative area that is being illuminated, part of the photogenerated current can be drained through the shunting load[55]. The EQE measurements (figure 3.18) revealed that the solar cells with the modification at the rear, Mo/Pt/SiO2, and Mo/Pd/SiO2, Mo/SiO2, have an increased quantum efficiency, being that translated into an increase in the J_{SC} when in comparison with reference solar cell. This occurrence may indicate that the sidewalls' height for the modified cells have a major influence on the formation of shunt paths, thus decreasing the performance of those cells, when compared with the reference.

Additionally, it was seen that the J_{SC} calculated from the J-V curve differed significantly from the simulations previously made in **section 3.1.2** by a difference of 12.01 mA/cm^2. As mention above, the optical simulations only consider optical losses rather than electrical ones, meaning that this reduction in J_{SC} current was probably associated with the latter. From a broad variety of electrical losses, the most likely cause is the high interface recombination at the rear contact, a typical problem associated with ultrathin film solar cells that do not possess a passivation layer. From **table 5**, it is possible to see that most of the solar cells followed approximately the same trend across all figures of merit. The exception is in the J_{SC}, with the Mo/Pt/SiO_2 and the Mo/SiO_2 exhibiting a major increase, when in comparison with the reference. Additionally, the difference between those two cells, regarding the efficiency, was of 0.21%. Being the only difference between them the layer of Pt in the first, this increase can be attributed to the reflection of light at the rear. Moreover, the observed increase of the J_{SC} for the cells with a passivation layer is well known and it is in accordance with several studies, where that layer leads to a reduction of the interface defects and to the generation of a built-in electric field that drives the minority carriers away from the rear contact [23–25].

It was also possible to observe a cross-over of the illuminated and dark curves for the solar cells with the metal in the rear contact, Mo/Pt/SiO_2 and Mo/Pd/SiO_2 (**figure 3.17**). This type of irregularity is normally associated either with the formation of an electron barrier or minority carrier recombination at the rear contact [55], thus being in accordance with what has been referred above.

Table 5 – Figures of merit of the fabricated solar cells.

Samples	V_{OC} [mV]	J_{SC} [mA/cm^2]	EQE J_{SC} [mA/cm^2]	FF [%]	Efficiency [%]
Mo/Pt/SiO_2	547±12	22.74±1.71	19.20±1.06	55.8 ±3.8	6.93±0.79
Mo/Pd/SiO_2	523±11	18.48±0.99	18.14±0.39	54.7±3.7	5.35±0.41
Mo/SiO_2	569±8	23.26±3.74	20.75±0.13	47.5±5.4	6.72±0.88
Reference	615±8	18.61±1.03	17.06±0.85	61.7±6.4	7.06±0.98

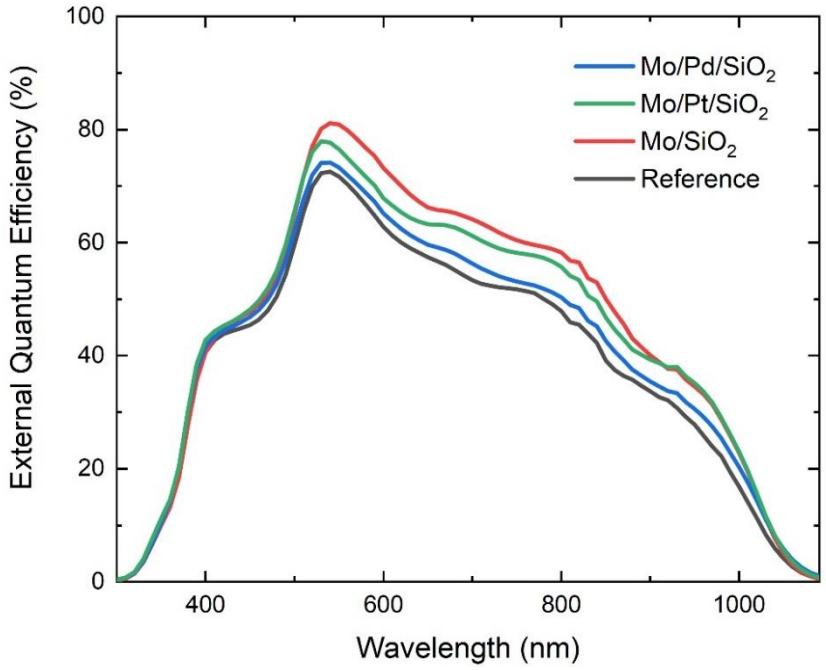

Figure 3.18 – External quantum efficiency measurements of the solar cells fabricated.

3.5 Alternative processes and architectures

In this section, two alternative structures explored in this work are presented with the objective to avoid the problems experienced with the fabrication shown in **figure 2.3**. Both alternative structures, name MACI simplified and Encapsulation, remain with the same purpose: increase the reflection at the rear of CIGS ultrathin film solar cells, therefore leading to an increase of the light absorbed.

The author would like to mention that only some initial tests were conducted, thus no solar cells were fabricated with none of these processes.

3.5.1 MACI

MACI is a variation of the process employed primarily in this work, therefore, the majority of the calibrations made in the primer can be used in this one. Here, the distinct anisotropic levels of the deposition processes were exploited in our benefit, in order to reach the final structure. At the same time, it was tried to simplify all the fabrication steps, without compromising the final result and facilitating a possible transition to industry. In **figure 3.19**, the fabrication steps were depicted.

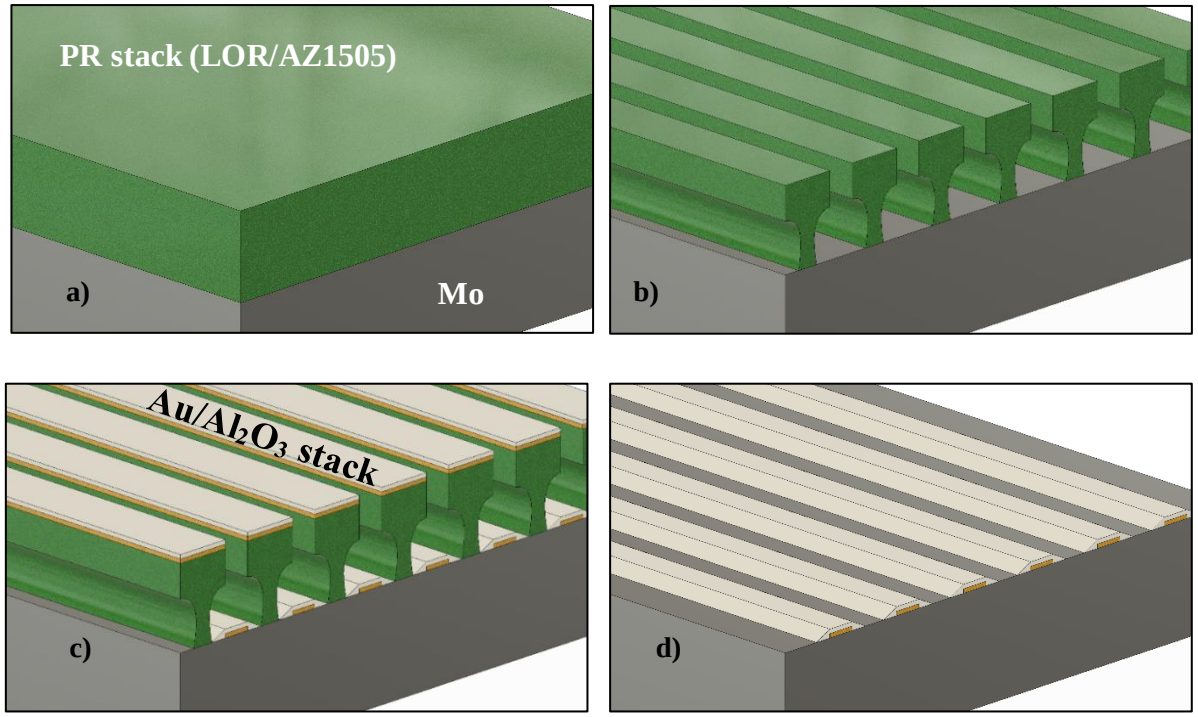

Figure 3.19 – The several steps regarding the fabrication process of the MACI structure. a) Photoresist stack coating, b) development, c) metal and insulator deposition, d) lift-off.

MACI starts with the deposition of the bilayer of photoresists (AZ1505 and LOR) on top of a SLG/MO stack (**figure 3.19a**). Thereafter, the sample was exposed and then developed (**figure3.19b**). In **figure 3.19c**, and **figure 3.19d**, the deposition of metal/dielectric, and the consequent lift-off can be seen. Already here, a slight difference between MACI and the main process used in this thesis is shown, considering that the lithographic step is done prior to deposition of the metal/insulator stack. Only with this adjustment, two benefits arise: **i,** an etch step is no longer required, saving time in calibrations needed for the several etch rates; **ii,** a second deposition of Mo required in order to encapsulate the metal and avoid its diffusion can be excluded, considering that the contact will be made under the photoresist and the metal will be completely covered by the insulator. Furthermore, with the removal of the second Mo, one interface disappears, what could hinder the recombination at the rear.

The key step in this procedure was the deposition of metal and dielectric. To see the viability of the process one simple and prompt test, from substrate to the desired rear structure (**figure 3.19d**) was conducted. For this study, the mask used had the exact same dimensions as the one used in **section 3.2.1**. The metal used was gold (20 nm) while the dielectric was alumina (10 nm). Based on previous studies from the group, it was known that the metal deposition using the Kenosistec (DC sputtering) was highly

anisotropic while the posterior deposition of dielectric using the FTM (RF sputtering) was conformal. Our objective was to make use of the undercut produced on the photoresist during the development to create an area where the dielectric deposition would encapsulate the metal, without the need to etch the second layer of Mo, as referred above.

Optical microscope images were taken between steps. **Figure 3.20a,** shows the sample after metal/dielectric deposition, while **figure 3.20b**, shows the sample after lift-off. These figures correspond to **figure 3.19c** and **figure 3.19d,** respectively.

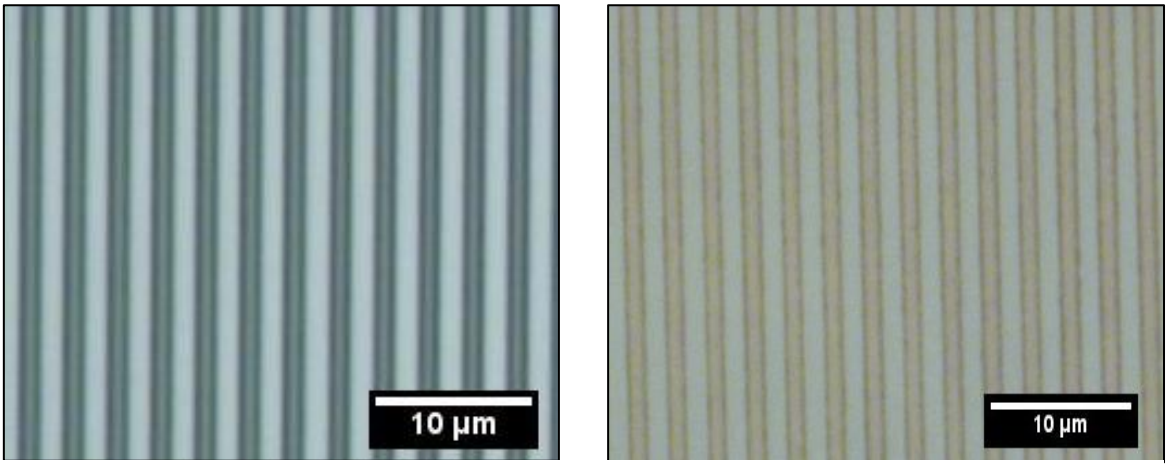

Figure 3.20 – Optical microscope images of MACI substrate a) after metal and dieletric deposition and b) after lift-off.

Both **figure 3.20a** and **figure 3.20b**, revealed no problems during any of steps. It is important to note once again that both steps were already well-calibrated in **section 3.2.2** and **section 3.2.4**, hence this result was expected. Afterwards a SEM (**figure 3.21**) cross-section analysis was also performed on the sample processed.

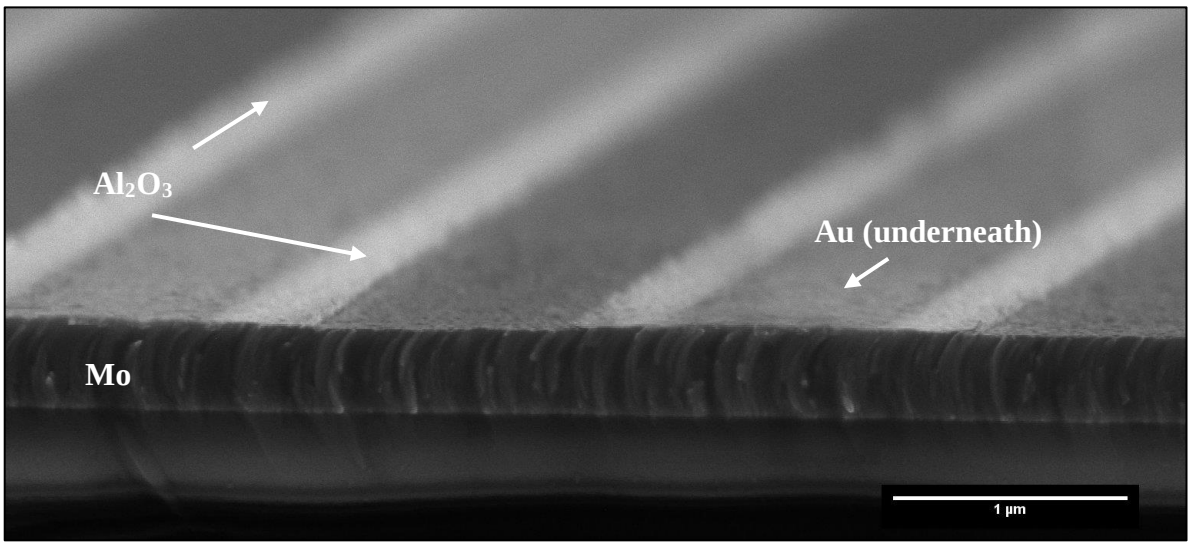

Figure 3.21 – SEM cross-section image of MACI substrate after lift-off.

The cross-section revealed a uniform pattern, completely in accordance with the optical microscope observations. Through **figure 3.21** it was possible to confirm that the Cu layer was in fact encapsulated with the Alumina layer. Additionally, it was verified, that even using the same mask used for the first structure, the passivated area increases substantially in comparison with the first. Notwithstanding the good results, alumina sidewalls with approximately 50 nm were found alongside the Mo contact. Being the deposition of Alumina highly conformal, it is normal to find these remnants. A good solution for this problem might be the use of a wet etchant after the fabrication, using, for example, the recipes found in [59]. Unfortunately, no further experiments could be performed in time to be presented in this work.

3.5.2 Encapsulation

The Encapsulation is a proof of concept for a novel nanostructure more complex than the other two previously discussed. This means that its transition to industry is not as straightforward as the others. The main reason for its complexity is the use of two E-beam lithographic steps, used to produce trenches. The trenches need to be aligned with each other in order for the encapsulation of the metal to be done properly. For that reason, it was necessary one more optical lithographic step to produce features that will guide the E-beam system (Vistec 5200 ES 100 kV) during the exposures in order for the alignment to be accurate.

As in the previous structure (**section 3.5.1**), here the process starts with an SLG substrate and a Mo layer on top of it, previously deposited in Uppsala. At INL, a 10 nm layer of metal (Au in our case) was deposited through DC sputtering (Kenosistec). Afterwards, AZ1505 photoresist was coated on top of the Au layer and then exposed in DWL. The mask used, creates four squares (20 µm x 20 µm) in each corner of the sample. The sample was then developed, and after, an etching step of 3 minutes was performed in order to create squared pits. These pits are the features that allow the alignment of the E-beam system. The AZ1505 resist was stripped using acetone in an ultrasonic bath for 5 minutes. Thereafter, a PMMA resist, specific for e-beam lithography, was coated on the sample. The first exposure took approximately 22 hours, and the pattern consisted of lines with 700 nm width and a pitch of 2 µm. After the development, the sample was etched for 45 seconds opening trenches through the gold **(figure 3.22a)**. The PMMA resist was then stripped and an Alumina layer with 20 nm was deposited through RF sputtering **(figure 3.22b)**. Next, a repetition of the lithographic step previously done was carried. Nevertheless, this time, the pattern exposed had 200 nm lines instead of the 700 nm, thus reducing the exposure time to 16 hours. It was of upmost importance that the second exposure was properly aligned with the first, considering that the correct encapsulation of the metal relied on that. For the alignment to happen, the system uses a drift correction option, that from time to time centers the electron beam with the squares on the corner and corrects its position relative to the first trenches exposed. After the second exposure, a new etch step was performed, in order to etch the dielectric, thus opening the trenches that will form the Mo contact with the CIGS absorber (**figure 3.22c**). The final step was the PMMA removal performing the same procedure used before.

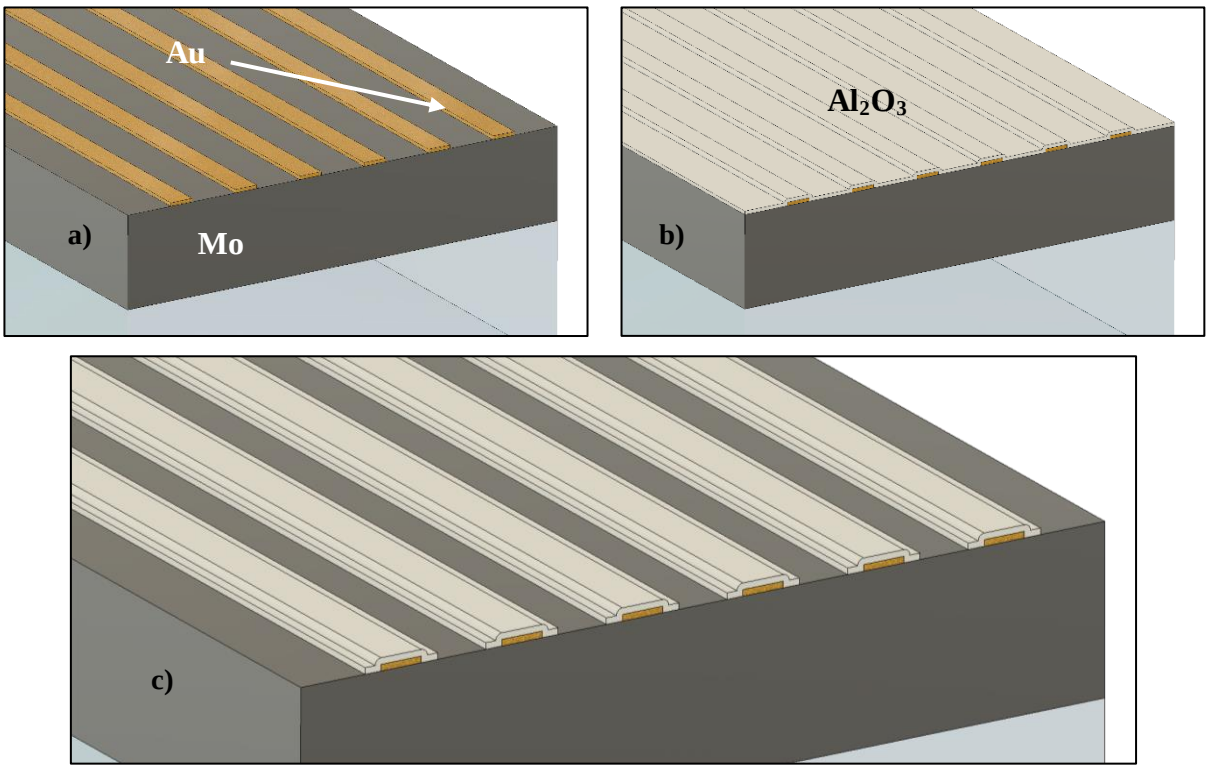

Figure 3.22 - The several steps regarding the fabrication process of the Encapsulation structure. a) Sample after the 1st E-beam lithography step, b) dielectric deposition, c) final structure after the 2nd E-beam lithography step.

3.5.2.1 E-beam dose calibration

In order to have the features with the correct sizes, a dose calibration was required, equivalent to the one made for the DWL laser intensity, referred in **section 3.2.1**. The calibration was performed by exposing PMMA photoresist, with a mask with different fields of 700 nm trenches. In each field a different exposure dose was used (from 450 to 1300 µC/cm^2). Afterwards, a SEM inspection allowed to make the measurements of the trenches produced in each field. By plotting a linear fit of the curve obtained, an average value of dose for the 700 nm trenches could be calculated. These results can be seen in **figure 3.23**. The analysis made lead to a dose value of 790 µC/cm^2. For the trenches with 200 nm, no calibration was required since it was made by our group in previous works, in a similar way.

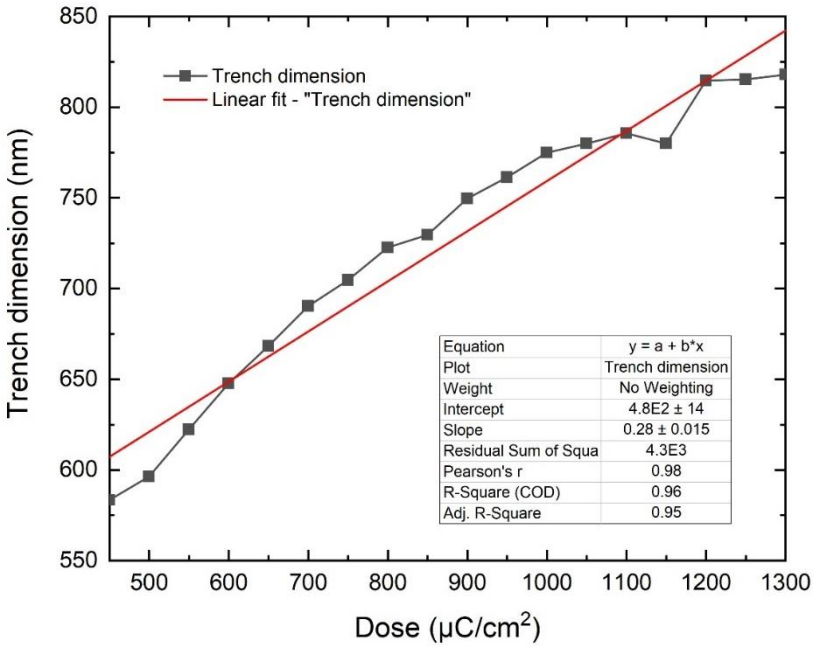

Figure 3.23 – Dose calibration curve of the E-beam system.

A first experiment was performed, with the fabrication of a sample following the procedure explained above. Afterwards, the sample was taken to the SEM, to verify if the metal was properly encapsulated. In **figure 3.24** it is possible to see how the E-beam exposure was done and the relative positions of the images taken with the SEM.

It is important to note that the inspection made could not be random. Although the E-beam system has a nanoscale accuracy with a drift correction option, the extremely long pattern that was exposed could lead to minor drifts of the beam that with time could become larger. For that reason, we took an SEM image at the beginning of the exposure (**figure 3.25 – X1**), and another when the exposure was almost finished (**figure 3.25 – X2**). Additionally, was performed an AFM analysis on the same locations of the sample (**figure 3.26**).

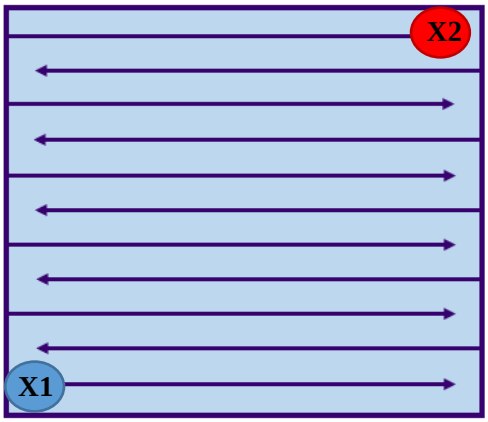

Figure 3.24 – Path of the E-beam during the exposure, being X1 where the exposure starts and X2 where it finishes

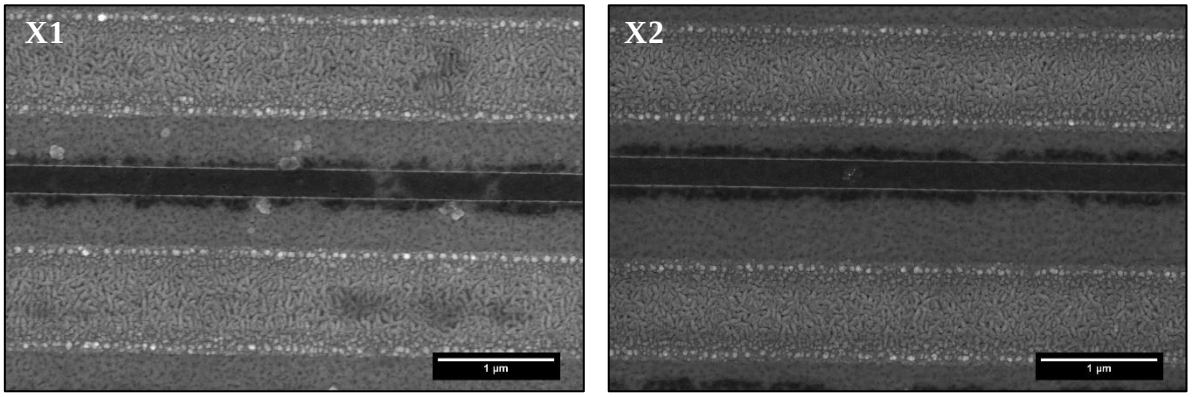

Figure 3.25 – SEM top-view image of the encapsulation sample fabricated. X1 was where the exposure starts while X2 where the exposure ends.

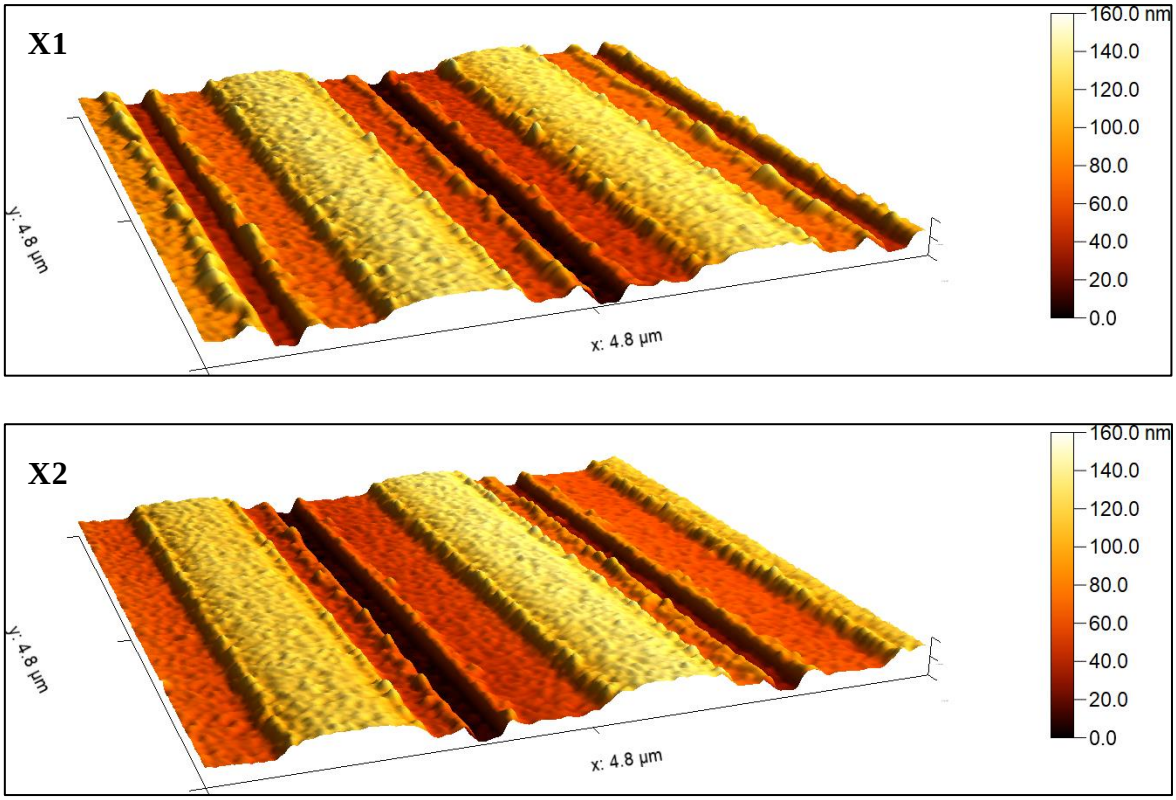

Figure 3.26 - AFM analysis of the encapsulation sample fabricated: X1 is where the exposure starts; X2 where the exposure finishes.

Through the use of both *ImageJ*, and *Gwyddion* softwares, it was possible to measure the drift deviation, as the exposure was done. In the area where the exposure began (figure x1), a deviation of approximately 20 nm was found, while where the exposure ended, the drift was of 160 nm, meaning that the encapsulation of the metal was properly done. It is important to note that although the E-beam system was using its drift correction option, a small deviation was expected considering the line's length.

These promising results open the possibility to the fabrication of solar cells. Nevertheless, since more experiments were required and considering that the samples had yet to be sent to Uppsala for the deposition of the remaining layers that compose the solar cell, no more conclusions were obtained in time to be presented in this thesis.

4. Conclusions and Future perspectives

The main objective of this thesis was to develop a working lift-off process for the fabrication of a novel structure on the rear contact of ultra-thin film CIGS solar cells. The goal of this novel structure was to increase the reflection on the rear contact of the cell through the use of a patterned metal layer (Cu, Ta, Pd, Pt). Additionally, that metal layer was required to be encapsulated with a dielectric (SiO_2), taking into account that, in previous studies from the group it was found that the metal could react with the CIGS layer, thus decreasing the cell overall performance. With that in mind, a photoresist, LOR 5B, specifically designed for lift-off was implemented on the fabrication process.

First, optical simulations made using *Lumerical* software allowed to identify the parasitic absorption on the rear contact as one of the main optical losses behind a thickness reduction from thin-film (1 µm) to ultrathin film (500 nm) CIGS solar cells. A J_{SC} loss of 2.52 mA/cm^2 was found with an increase of the parasitic absorption on the rear contact of 2.32 mA/cm^2. Afterwards, a promising solution with the implementation of a novel structure using several metals (Cu, Ta, Pd, Pt) was presented and simulated, revealing a J_{SC} increase of 1.06 mA/cm^2 (for the Cu), when in comparison with a reference. Nevertheless, it was also seen that although an enhancement was observed, it was not possible to match the absorption of the standard 1 µm solar cell. Notwithstanding the fact that more light is being reflected on the metal at the rear, most of that light is not being absorbed in the second pass through the absorber. As expected, a decrease of the parasitic light absorption at the rear by the introduction of a rear mirror needs to be accompanied by the introduction of other light management strategies that allow to increase the optical path even further.

INL's equipment and facilities are not calibrated to work with 5 by 5 cm^2 substrates neither to fabricate sub-micrometer features. For that reason, the calibrations made in this thesis were of upmost importance and a key component of this work, showing that standard microelectronic processes can be used to process glass substrates exactly the same as the ones used in current solar modules, allowing for an industrial upscaling of the technology developed here. On top of that, the calibrations allowed us to simplify our process and, simultaneously, avoid fabrication errors. Nevertheless, after the calibrations and posterior fabrication of our samples, a SEM and AFM analysis revealed a 200 nm deposition of Mo outside the previously etched trenches and as a consequence, the appearance of Mo sidewalls with 50 (Mo/SiO_2) to 60 ($Mo/Pt/SiO_2$ and $Mo/Pd/SiO_2$) nm height. Through another experiment, it was concluded that this Mo deposition happened because the sputtering deposition of Mo was slightly isotropic, while the RIE revealed trenches with near-perfect vertical walls. Through 3D topographic images, it was seen that an effective reduction of the active area of reflection and passivation had occurred, reaching an average value of 30%. Additionally, the profiles obtained through those topographic images confirmed that with the sidewalls and the 200 nm overextension of Mo alongside the lines, the reduction of the interface recombination would be problematic since the contact area was still very high for the passivation to occur. Nonetheless, through spectrophotometry, it was seen that this unintended pattern previously created, had an impressive increase in the diffuse reflectance, with relative average values of 13%, between 1050 and 1100 nm wavelengths, and for that reason it was decided to proceed with the fabrication.

The J-V and EQE measurements revealed that the best cell was the $Mo/Pt/SiO_2$, with an efficiency of 6.93%. Moreover, an increase of the J_{SC} for the $Mo/Pt/SiO_2$ and Mo/SiO_2 was observed, with the Mo/SiO2 reaching an increase of 4.65 mA/cm2, in comparison with the reference. (…) At the same time the low VOC and FF for the modified solar cells might indicate that those cells have an increased rear contact recombination. Another important conclusion was that all the solar cells survived during the CIGS deposition, meaning that the encapsulation was successful, and there was no diffusion of metal during that process.

In the future, the process used to fabricate the main structure presented in this work still requires some optimization. That can be done in several ways: **i)** by reducing the LOR 5B thickness, thus

reducing the undercut height, what could lead to a smaller quantity of Mo deposited alongside the trenches; **ii)** through the increase of the size of the AZ1505 photoresist, also leading to a minor quantity of Mo deposited below the undercut; **iii)** changing the undercut size, for instance, reducing the development time. Unfortunately, none of these tests were performed due to the lack of time. Despite that, two alternative structures were also presented (MACI and Encapsulation), with very promising results.

5. References

[1] W. Shockley and H. J. Queisser, "Detailed Balance Limit of Efficiency of *p-n* Junction Solar Cells," *J. Appl. Phys.*, vol. 32, no. 3, pp. 510–519, Mar. 1961.

[2] *World Energy Outlook 2018*. OECD, 2018.

[3] M. A. Green *et al.*, "Solar cell efficiency tables (Version 53)," *Prog. Photovoltaics Res. Appl.*, vol. 27, no. 1, pp. 3–12, Jan. 2019.

[4] K. Mertens, *Photovoltaics Fundamentals, Technology, and Practice*. John Wiley & Sons, Incorporated, 2018.

[5] S. M. Sze and K. K. Ng, *Physics of semiconductor devices*. Wiley-Interscience, 2007.

[6] J. Lindahl, "Atomic layer deposition of zinc tin oxide buffer layers for Cu(In,Ga)Se 2 solar cells," 2015.

[7] G. B. Gharehpetian, S. M. Mousavi Agah, K. Ramalingam, and C. Indulkar, "Solar Energy and Photovoltaic Technology," *Distrib. Gener. Syst.*, pp. 69–147, Jan. 2017.

[8] J. Schöldström, "Thermal Radiation from Co-evaporated Cu(In,Ga)Se2 : End point detection and process control," 2012.

[9] S. S. Hegedus and W. N. Shafarman, "Thin-film solar cells: device measurements and analysis," *Prog. Photovoltaics Res. Appl.*, vol. 12, no. 23, pp. 155–176, Mar. 2004.

[10] J. L. Shay, S. Wagner, and H. M. Kasper, "Efficient CuInSe $_2$ /CdS solar cells," *Appl. Phys. Lett.*, vol. 27, no. 2, pp. 89–90, Jul. 1975.

[11] N. Naghavi *et al.*, "Ultrathin Cu(In,Ga)Se2 based solar cells," *Thin Solid Films*, vol. 633, pp. 55–60, Jul. 2017.

[12] R. Scheer and H. W. (Hans-W. Schock, *Chalcogenide photovoltaics : physics, technologies, and thin film devices*. Wiley-VCH, 2011.

[13] T. D. Lee and A. U. Ebong, "A review of thin film solar cell technologies and challenges," *Renew. Sustain. Energy Rev.*, vol. 70, pp. 1286–1297, Apr. 2017.

[14] "Solar Frontier Achieves World Record Thin-Film Solar Cell Efficiency of 23.35%." [Online]. Available: https://www.enfsolar.com/news/15569/solar-frontier-achieves-world-record-thin-film-solar-cell-efficiency-of-23-35. [Accessed: 29-Jul-2019].

[15] L. M. Mansfield *et al.*, "Efficiency increased to 15.2% for ultra-thin Cu(In,Ga)Se $_2$ solar cells," *Prog. Photovoltaics Res. Appl.*, vol. 26, no. 11, pp. 949–954, Nov. 2018.

[16] K. Counts, "Comparative analysis of Cu(InGa)Se2 solar cells," 2016.

[17] S. Suresh, "Back to Ground Zero: A study on rear passivated thin-CIGS solar cells." 2018.

[18] K. H. Ong *et al.*, "Review on Substrate and Molybdenum Back Contact in CIGS Thin Film Solar Cell," *Int. J. Photoenergy*, vol. 2018, pp. 1–14, Sep. 2018.

[19] R. Mohan and R. Paulose, "Brief Review on Copper Indium Gallium Diselenide (CIGS) Solar Cells," in *Photoenergy and Thin Film Materials*, Hoboken, NJ, USA: John Wiley & Sons, Inc., 2019, pp. 157–192.

[20] D. Hariskos, S. Spiering, and M. Powalla, "Buffer layers in Cu(In,Ga)Se2 solar cells and modules," *Thin Solid Films*, vol. 480–481, pp. 99–109, Jun. 2005.

[21] P. M. B. C. Salvador, "Deposition and characterization of CdS and ZnO:Al thin films for Cu(In,Ga)Se solar cells," Jan. 2016.

[22] J. Lindahl *et al.*, "Inline Cu(In,Ga)Se$_{2}$ Co-evaporation for High-Efficiency Solar Cells and Modules," *IEEE J. Photovoltaics*, vol. 3, no. 3, pp. 1100–1105, Jul. 2013.

[23] F. Mollica, "Optimization of ultra-thin Cu(In,Ga)Se2 based solar cells with alternative back-contacts," Dec. 2016.

[24] J. . Guillemoles, "The puzzle of Cu(In,Ga)Se2 (CIGS) solar cells stability," *Thin Solid Films*, vol. 403–404, pp. 405–409, Feb. 2002.

[25] J. Ramanujam and U. P. Singh, "Copper indium gallium selenide based solar cells – a review," *Energy Environ. Sci.*, vol. 10, no. 6, pp. 1306–1319, Jun. 2017.

[26] K. A. W. Horowitz and M. Woodhouse, "Cost and potential of monolithic CIGS photovoltaic modules," *2015 IEEE 42nd Photovolt. Spec. Conf. PVSC 2015*, vol. 2, pp. 1–6, 2015.

[27] O. Lundberg, M. Bodegård, J. Malmström, and L. Stolt, "Influence of the Cu(In,Ga)Se $_2$ thickness and Ga grading on solar cell performance," *Prog. Photovoltaics Res. Appl.*, vol. 11, no. 2, pp. 77–88, Mar. 2003.

[28] Z. J. Li-Kao *et al.*, "Towards ultrathin copper indium gallium diselenide solar cells: proof of concept study by chemical etching and gold back contact engineering," *Prog. Photovoltaics Res. Appl.*, vol. 20, no. 5, pp. 582–587, Aug. 2012.

[29] P. M. P. Salomé *et al.*, "Passivation of Interfaces in Thin Film Solar Cells: Understanding the Effects of a Nanostructured Rear Point Contact Layer," *Adv. Mater. Interfaces*, vol. 5, no. 2, p. 1701101, 2018.

[30] B. Vermang *et al.*, "Highly reflective rear surface passivation design for ultra-thin Cu(In,Ga)Se2 solar cells," *Thin Solid Films*, vol. 582, pp. 300–303, 2015.

[31] G. Rajan *et al.*, "Optimization of anti-reflective coatings for CIGS solar cells via real time spectroscopic ellipsometry," *2015 IEEE 42nd Photovolt. Spec. Conf. PVSC 2015*, no. 1, pp. 4–7, 2015.

[32] T. Lopes *et al.*, "Rear Optical Reflection and Passivation Using a Nanopatterned Metal/Dielectric Structure in Thin-Film Solar Cells," *IEEE J. Photovoltaics*, vol. PP, pp. 1–7, 2019.

[33] S. Morawiec, M. Mendes, S. Mirabella, F. Simone, F. Priolo, and I. Crupi, "Self-assembled silver nanoparticles for plasmon-enhanced solar cell back reflectors: Correlation between structural and optical properties," *Nanotechnology*, vol. 24, p. 265601, 2013.

[34] E. D. Palik, *Handbook of optical constants of solids*, vol. 1. Elsevier Inc., 2012.

[35] P. D. Paulson, R. W. Birkmire, and W. N. Shafarman, "Optical characterization of CuIn1-xGaxSe2 alloy thin films by spectroscopic ellipsometry," *J. Appl. Phys.*, vol. 94, no. 2, pp. 879–888, Jul. 2003.

[36] M. Dhankhar, O. Pal Singh, and V. N. Singh, "Physical principles of losses in thin film solar cells and efficiency enhancement methods," *Renew. Sustain. Energy Rev.*, vol. 40, pp. 214–223, Dec. 2014.

[37] T. Kato, J.-L. Wu, Y. Hirai, H. Sugimoto, and V. Bermudez, "Record Efficiency for Thin-Film Polycrystalline Solar Cells Up to 22.9% Achieved by Cs-Treated Cu(In,Ga)(Se,S) $_2$," *IEEE J. Photovoltaics*, vol. 9, no. 1, pp. 325–330, Jan. 2019.

[38] M. D. Heinemann *et al.*, "Advantageous light management in Cu(In,Ga)Se2 superstrate solar cells," *Sol. Energy Mater. Sol. Cells*, vol. 150, pp. 76–81, Jun. 2016.

[39] B. Vermang *et al.*, "Highly reflective rear surface passivation design for ultra-thin Cu(In,Ga)Se2 solar cells," *Thin Solid Films*, vol. 582, pp. 300–303, May 2015.

[40] B. Lin, "Processing and Optimization," in *Optical Lithography*, 1000 20th Street, Bellingham, WA 98227-0010 USA: SPIE, pp. 213–322.

[41] C. A. Mack, *Fundamental principles of optical lithography : the science of microfabrication*. Wiley, 2007.

[42] M. J. Madou, *Fundamentals of microfabrication and nanotechnology*. CRC Press, 2012.

[43] T. Grimsley and S. O'Brien, "Metal Lift-off Using a Bi-layer Process - SMFL - RIT Wiki." [Online]. Available: https://wiki.rit.edu/display/smfl/Metal+Lift-off+Using+a+Bi-layer+Process. [Accessed: 22-Aug-2019].

[44] K. T. Chung, J. H. Reisner, and E. R. Campbell, "Charging phenomena in the scanning electron microscopy of conductor-insulator composites: A tool for composite structural analysis," *J. Appl. Phys.*, vol. 54, no. 11, pp. 6099–6112, Nov. 1983.

[45] K. H. Kim, Z. Akase, T. Suzuki, and D. Shindo, "Charging Effects on SEM/SIM Contrast of Metal/Insulator System in Various Metallic Coating Conditions," *Mater. Trans.*, vol. 51, no. 6,

pp. 1080–1083, 2010.

[46] *Advanced characterization techniques for thin film solar cells*. .

[47] "PMGI & LOR Lift-off Resists - MicroChem." [Online]. Available: http://microchem.com/Prod-PMGI_LOR.htm. [Accessed: 28-Aug-2019].

[48] V. Lindroos, M. Tilli, A. Lehto, T. Motooka, S. Franssila, and S. Tuomikoski, "MEMS Lithography," *Handb. Silicon Based MEMS Mater. Technol.*, pp. 333–348, Jan. 2010.

[49] B. GOROWITZ and R. J. SAIA, "Reactive Ion Etching," *VLSI Electron. Microstruct. Sci.*, vol. 8, pp. 297–339, Jan. 1984.

[50] S.-K. Lee, S.-S. Chun, C. Hwang, and W.-J. Lee, "Reactive Ion Etching Mechanism of Copper Film in Chlorine-based Electron Cyclotron Resonance Plasma," *Jpn. J. Appl. Phys.*, vol. 36, no. Part 1, No. 1A, pp. 50–55, Jan. 1997.

[51] H. Ekinci, "Plasma and Reactive Ion Etching," *Ref. Modul. Mater. Sci. Mater. Eng.*, Jan. 2016.

[52] O. Lundberg, M. Bodegård, J. Malmström, and L. Stolt, "Influence of the Cu(In,Ga)Se_2 thickness and Ga grading on solar cell performance," *Prog. Photovoltaics Res. Appl.*, vol. 11, no. 2, pp. 77–88, Mar. 2003.

[53] M. Schmid, "Review on light management by nanostructures in chalcopyrite solar cells," *Semicond. Sci. Technol.*, vol. 32, no. 4, p. 043003, Apr. 2017.

[54] S. Morawiec *et al.*, "Broadband photocurrent enhancement in a-Si:H solar cells with plasmonic back reflectors," *Opt. Express*, vol. 22, no. S4, p. A1059, Jun. 2014.

[55] R. Scheer and H. W. (Hans-W. Schock, *Chalcogenide photovoltaics : physics, technologies, and thin film devices*. Wiley-VCH, 2011.

[56] S. Bose *et al.*, "Optical Lithography Patterning of SiO_2 Layers for Interface Passivation of Thin Film Solar Cells," *Sol. RRL*, vol. 2, no. 12, p. 1800212, Dec. 2018.

[57] D. Ledinek, P. Salome, C. Hagglund, U. Zimmermann, and M. Edoff, "Rear Contact Passivation for High Bandgap Cu(In, Ga)Se Solar Cells With a Flat Ga profile," *IEEE J. Photovoltaics*, pp. 1–7, 2018.

[58] P. M. P. Salomé *et al.*, "Passivation of Interfaces in Thin Film Solar Cells: Understanding the Effects of a Nanostructured Rear Point Contact Layer," *Adv. Mater. Interfaces*, vol. 5, no. 2, p. 1701101, Jan. 2018.

[59] "Preparation and Microstructural Analysis of High-Performance Ceramics," in *Metallography and Microstructures*, ASM International, 2004, pp. 1057–1066.

6.1 Simulated structures

-The simulated reference solar cell:

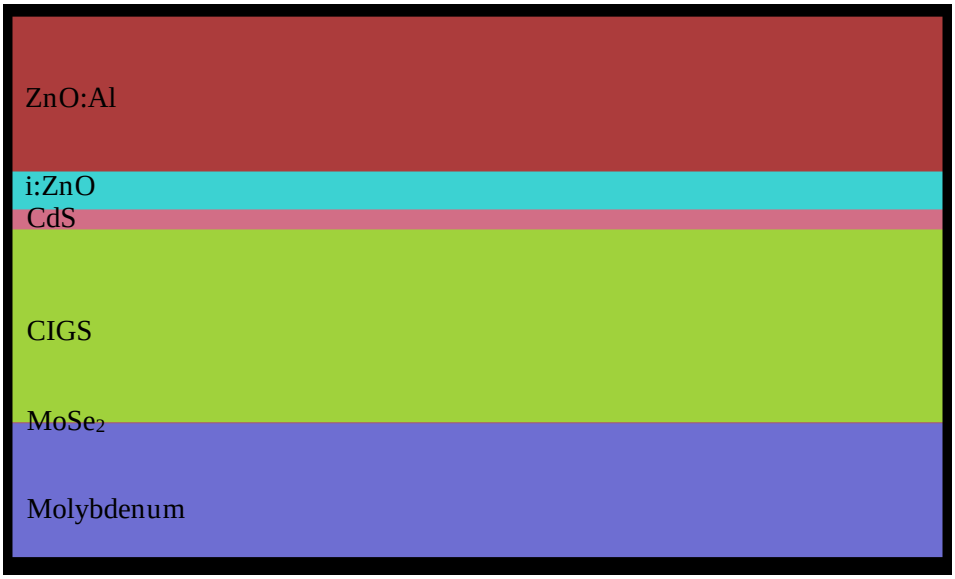

-Implementation of the novel structure with the metal on the solar cell simulations (in this case the cell depicted used Pt, as example.

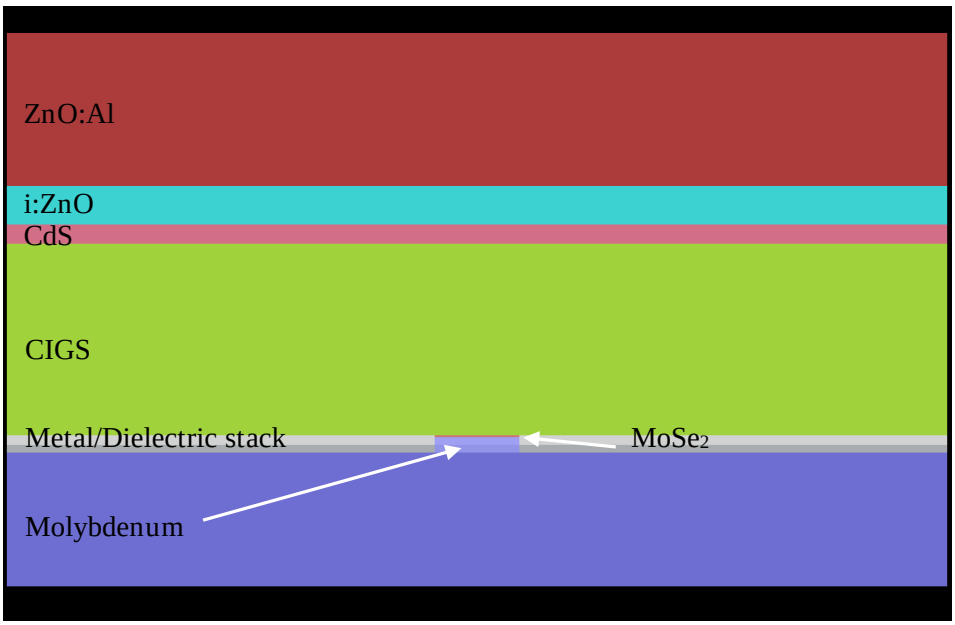

Figure 6.1 – Simulated structures on *Lumerical*.

6.2 SEM Measurements

All the measurements presented in this thesis regarding SEM images were made using ImageJ software. As an example, the measurements made to figure X are shown here:

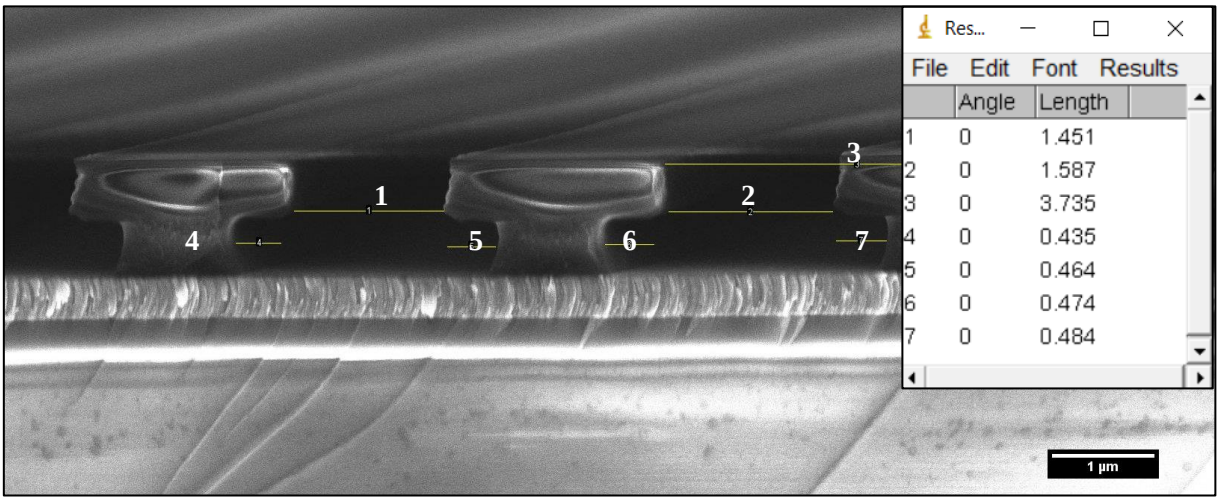

6.3 AFM – Profile measurements

Using Gwyddion the profile of the samples was obtained. Afterwards, Imagej was used to calculate the features desired. In this case, an example of the measurements made to calculate the sidewalls' height (figure 3.12) is depicted.

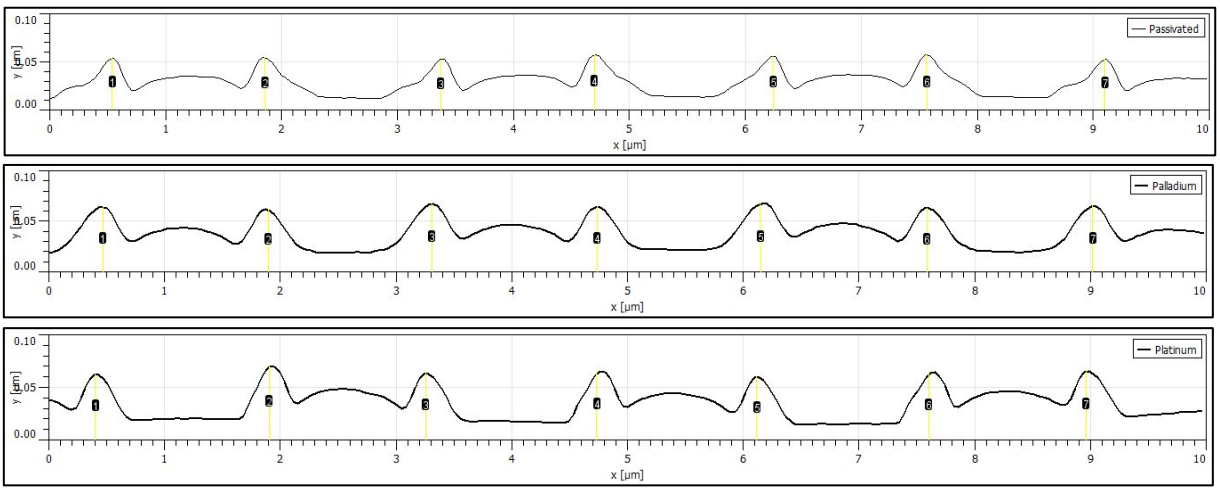

Passivated	Palladium	Platinum

	Angle	Length
1	90	5.386
2	90.971	5.589
3	90.000	5.340
4	90.000	5.808
5	90.955	5.644
6	90.924	5.761
7	90.000	5.293

	Angle	Length
1	90	0.065
2	90	0.063
3	90	0.068
4	90	0.065
5	90.744	0.069
6	90.000	0.064
7	90.000	0.066

	Angle	Length
1	90	0.063
2	90	0.071
3	90	0.064
4	90	0.066
5	90	0.061
6	90	0.065
7	90	0.066

6.4 Paper publication

J. M. V.Cunha *et al.*, "Decoupling of Optical and Electrical Properties of Rear Contact CIGS Solar Cells", *IEEE Journal of Photovoltaics*, 2019. DOI: 10.1109/JPHOTOV.2019.2933357

***Abstract*—A novel architecture that comprises rear interface passivation and increased rear optical reflection is presented with the following advantages: i) enhanced optical reflection is achieved by the deposition of a metallic layer over the Mo rear contact; ii) improved interface quality with CIGS by adding a sputtered Al_2O_3 layer over the metallic layer; and, iii) optimal ohmic electrical contact ensured by rear-openings refilling with a second layer of Mo as generally observed from the growth of CIGS on Mo. Hence, a decoupling between the electrical function and the optical purpose of the rear substrate is achieved. We present in detail the manufacturing procedure of such type of architecture together with its benefits and caveats. A preliminary analysis showing an architecture proof-of-concept is presented and discussed.**

***Index Terms*—Cu(In,Ga)Se_2 (CIGS), passivation, semiconductors, ultrathin.**

I. Introduction

Nowadays, absorber layers of Cu(In,Ga)Se_2 (CIGS) with sub-micrometer thicknesses, or ultrathin absorbers, are one of the main thin-film solar cell research topics. In addition to a lower material cost due to its usage reduction, the bulk recombination

rate within the CIGS absorber layer may also decrease [1]–[3]. With these two potential benefits, research work has been focused on solving two inherent problems entailed by the use of ultrathin photovoltaic technology: i) increased rear interface recombination at the Mo/CIGS interface, and ii) abridged photogeneration due to the necessary width for full absorption being effectively larger than the absorber thickness. In other words, the light path is significantly shorter than the absorption

length. Despite the presence of rear interface recombination in thick films, the effect is more pronounce in ultrathin devices. Such recombination losses are higher in ultrathin devices as a larger share of the minority charge carriers are generated

closer to the rear contact as compared with standard thick CIGS devices. A solution to mitigate such problems is the use of a structure located between the rear contact and the CIGS layer comprising a dielectric passivation layer with point contacts [1], [4]–[7]. The main limitation of this approach is that the point contacts need to occupy an area as small as possible, while, at the same time, being located within distances close enough to avoid resistive losses [8]. This compromise means that the gap between two contacts needs to be in a range of 1–4 μm. In order to decrease the contact area, the opening diameters should be limited from 100 to 400 nm. Hence, recent works have been dealing with the determination of the most suitable dielectric material to be used among Al_2O_3, SiO_2, Si_3N_4, HfO_2, etc. [1], [5], [6], [9] as well as with the determination of the most suitable patterning approach [4], [6], [10]–[12]. Until now, e-beam lithography of atomic layer deposited (ALD) Al_2O_3 has been the benchmark of the performed studies [4], and optical lithography of line contacts has shown positive results with the benefit of being more industrial friendly [8]. With regards to optical losses, several approaches have been tested with different outcomes. Z. J. Li-Kao *et al.* [13] developed an ingenious but complex CIGS lift-off process that moves the CIGS into an Au substrate allowing for an ohmic contact with excellent reflective properties [14], [15]. However, the procedure seems to be very complex for industrial application. The replacement of Mo by other metals with higher reflection is yet to be achieved mostly due to metal out-diffusion to the CIGS, selenization of the metal, or poor electrical contact [16], [17]. Moreover, part of the difficulty with the increase off the rear optical reflection is related to the coupling of the optical property of this layer with the electrical contacts. Empirically, Mo is known to be the unique solution [18] due, among other things, to the suppression of Se diffusion and the formation of a very thin MoSe2 layer, enhancing a good ohmic contact [19]. Hence, an ideal rear contact architecture for ultrathin CIGS solar cells would need to have:

i) Mo as the electrical contact;
ii) high optical reflection; and
iii) an additional passivation strategy.

For these objectives to be met, a decoupling of the optical properties with the electrical properties of the rear contact is required. In this work, we present a process that merges the Mo point contact structure with a metal reflective layer. This approach ensures that the contacts occupying a small percentage of the interface area are made of Mo, allowing for a good ohmic contact. The rest of the area is left with the passivation material and underneath a highly reflective material that further reduces the optical losses of ultrathin devices. Furthermore, Mo will prevent Se diffusion into the metallic interlayers, and, therefore, serve also as a diffusion barrier.

II. Experimental

In this section, we will present the fabrication procedure of the studied devices with the exception of the new architecture that will be presented in detail in the next section. The standard CIGS solar cell stack is soda-lime-glass (SLG)/Mo/CIGS/CdS/i:ZnO/ZnO:Al with Ni/Al/Ni as front contacts [20]. With the exception of our reference device, an evaporated 15-nm sodium fluoride (NaF) precursor layer was deposited on the top of the rear contact structure just prior to the CIGS growth [21]. The average thickness of the CIGS layer, which was measured using stylus profilometry, is (0.62 $\pm$ 0.05) μm with the compositional values of [Cu]/([Ga]+[In])=0.88 $\pm$ 0.02 and [Ga]/([Ga]+[In])=0.31 $\pm$0.01, which was measured using X-ray fluorescence. Ungraded (flat profile evaporation rates) CIGS absorbers were used for our experiments [4], [22],[23], with a growth temperature of 550 °C. The metal diffusion can be significant due to the high processing temperature used

during the CIGS growth. Twelve individual solar cells were defined with an area of 0.5 cm_2, as described elsewhere [20]. To study the electrical behavior of the solar cells, illuminated current density versus voltage (J–V) at AM1.5 and external quantum efficiency (EQE) measurements were performed in home-built systems. Simulations of the solar cells were done using a numerical three-dimensional mesh-based finite-difference

time-domain (FDTD) method to model the optical response of the fabricated structures, employing a specialized commercial solver [4], [17]. A focused ion beam, Helios NanoLab 450s from FEI, was used to prepare the cross-section samples for the

transmission electron microscopy (TEM) analysis. The lamella polishing was finished with a low Ga-ion accelerating voltage, below 2 kV. The TEM study was performed at 200 kV on a Titan (G3) Cubed Themis from FEI, utilizing the software Esprit from Bruker. The samples description and name used hereafter are presented in Table I. A reference ultrathin (A) and a passivation reference (B) were fabricated. Moreover, to validate the benefits

of the lift-off process, two samples with a Ta interlayer were produced. One sample with a simple Ta interlayer, Mo/Ta/Al_2O_3 (sample C), is studied.Asecond sample with the lift-off process, where Ta is the interlayer and in addition there is Mo inside the line contacts (sample D), is also studied, as depicted in Fig. 1.

III. Proposed Architecture and Processing Steps

The novel architecture is schematically shown in Fig. 1. For a proof-of-concept, we use line contacts instead of point contacts, as the point contact process is more complex and time-consuming, and the line contacts are industrially scalable using conventional optical lithography. The dimensions of the lines and their spacing can lead easily to contact resistance losses (seen in V_{oc} and FF losses) and, therefore, their design requires special attention [8]. Hence, 700 nm lines spaced by a 2.8 μm pitch are used in this article, as they are known to reduce the rear-interface recombination velocity [8]. We will use Ta as the interlayer for several reasons:

TABLE I
Samples Description and Respective Naming

Substrate	Description
SLG/Mo	(A) Mo reference
SLG/Mo/ns-Al_2O_3	(B) Passivation reference
SLG/Mo/Ta/ns-Al_2O_3	(C) Ta interlayer
SLG/Mo/Ta/ns-Al_2O_3/Mo	(D) Lift-off process with Mo filling the contacts

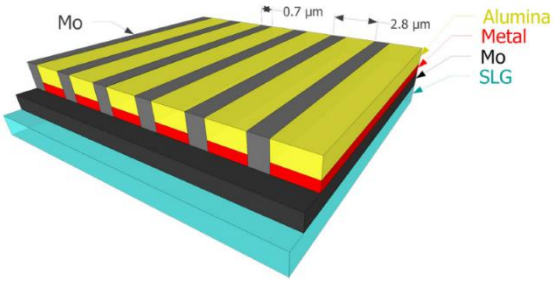

Fig. 1. Schematic representation of the developed architecture with Mo filling the line contacts.

i) theoretically, as shownin Section IV-B, it has the potential to reflect more light than the standard structure;

ii) if not fully encapsulated, it will heavily degrade CIGS performance through elemental in- and out-diffusion [7];

and

iii) we can etch vertical structures inside Ta using the same reactive ion etching procedure used for the opening of the Al_2O_3 structures.

The photolithography steps necessary for the substrate fabrication are depicted in Fig. 2 and commented in Table II. The lithographic definition is done using optical lithography, and the Al2O3 is open with a reactive ion etch step. Ideally, the etching opens both the Al2O3 and the metal layer. At this point, the photoresist is kept, and the secondMolayer is deposited. The lift-off allows for Mo to be kept inside the line contacts leaving the Al2O3 layer exposed.

IV. Results

A. Morphological Analysis

To demonstrate that the lift-off process used in sample D: i) prevents Se diffusion; and ii) allows for the contact lines to be cleaned from Al_2O_3 and Ta, we performed EDS analysis in a TEM cross-section image. Fig. 3 shows the EDS maps for Mo, Al, Ta, Se, and Cu. The EDS analysis was performed at the border between a line contact and the Ta/Al_2O_3 insulated area. The analysis shows:

i) there is no Se diffusion into the Al_2O_3, or inside the line contact, demonstrating that the second Mo layer prevents Se diffusion;

ii) the lift-off Mo layer inside the line contact superimposes the line edge, further preventing lateral diffusion; and

iii) the etching process fully removes Al from the line contact allowing for electrical contact.

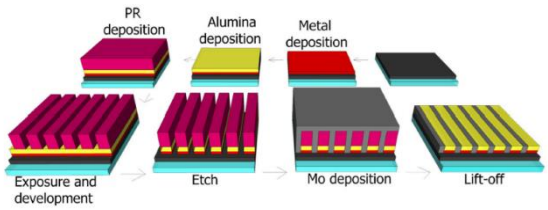

Fig. 2. Schematic representation of the photolithography process used for the formation of the line contacts and the deposition of Mo inside. PR is an acronym for Photoresist.

TABLE II
DETAILED DESCRIPTION OF THE CLEAN ROOM PROCESSING OF THE LIFT-OFF PROCESS THAT PROVIDES FOR A LINE CONTACT STRUCTURE FILLED WITH MO

Step	Description	Properties
0	SLG substrate	Cleaning by ultrasounds and detergent in H_2O
1	Mo rear contact deposition	Bilayer Mo, DC-sputtering - 350 nm total thickness
2	Metallic layer deposition	DC Sputtering - 10 nm
3	Passivation layer deposition	RF sputtering - 18 nm
4	Contact lines creation by direct laser write exposure	• HMDS (hexamethyldisilazane) vapor priming • Deposition of photoresist by spin coating • Laser exposure • Pattern development
5	Opening of the contact lines	Dry etching using reactive ion etching (ICP)
6	Mo deposition in the lines	DC-Sputtering - 30 nm
7	Lift-off	Ultrasounds in an acetone bath
8	Surface cleaning	O_2 Plasma treatment
9	Solar cell fabrication	Angstrom Solar cell Baseline [20]

This analysis, in particular, leaves open the possibility that some Ta remains inside the line contact. Despite considering that these Ta residues form a very thin layer trapped in-between Mo, we performed an EDS line scan in the middle of the line contact. The EDS line scan measurements for outside the line contact and inside the line, respectively, are shown in Figs. 4 and 5. Both EDS line scans show very well-defined structures, which withstood the harsh CIGS co-evaporation process. Furthermore, Fig. 5 shows no presence of Ta in the line contact, evidencing that we have the expected Mo/Mo/CIGS structure. Thus, an effective etching of Ta and Al_2O_3 and a successful second Mo deposition have been performed. We note that both analyses, and also the EDS mapping show a residual amount of Mo in the CIGS. Nonetheless, it is only a background signal emanating from the Mo TEM grid used for the study.

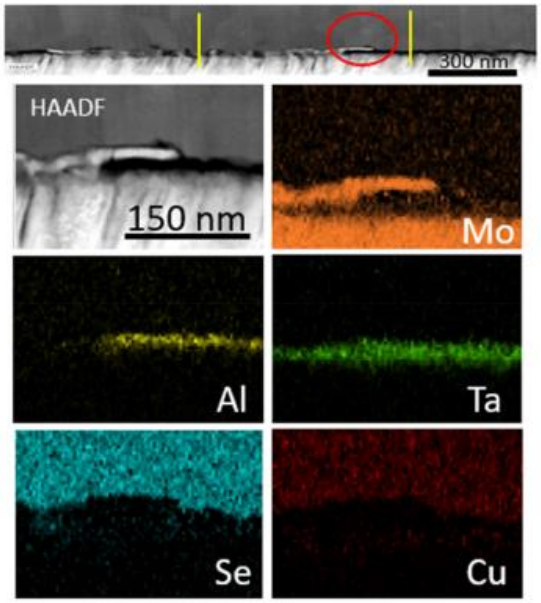

Fig. 3. TEM high angular annular dark-field image (HAADF) cross-section image and EDS mapping of sample D. The red circle corresponds to the EDS mapping area, whereas the vertical yellow lines correspond to the line scan regions.

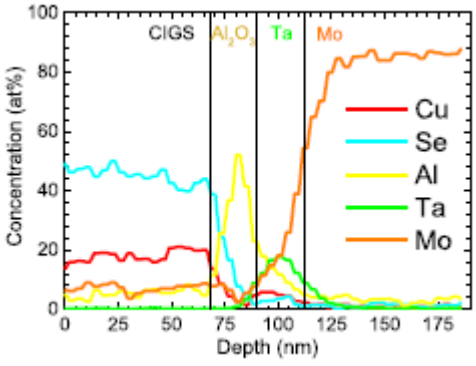

Fig. 4. EDS line scan passivated Mo/Ta/Al_2O_3/CIGS. The vertical lines are guides represent the layered passivation structure.

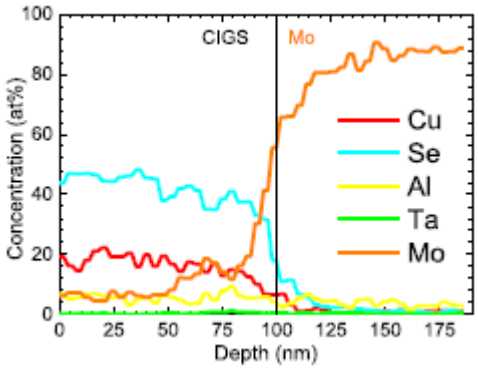

Fig. 5. EDS line scan Mo/CIGS inside line contact. The vertical lines represent the well-defined Mo/CIGS line contact.

B. Electrical Characterization

The *J–V* measurements are depicted in Fig. 6, and respective figures of merit are shown in Table III. Both *J–V* and EQE results (see Fig. 7) confirm the benefits of employing rear passivation by comparing a Mo reference (sample A) with a passivation reference (sample B), as expected and widely reported [1], [4], [6], [10], [17], [24]–[26]. Although the reference sample (A) shows a low average efficiency (5.4%), it is within the range of values presented in the literature. Ultrathin CIGS devices need different optimizations than the ones of regular CIGS thickness, and this fact causes runs to be more variable than their thick counterparts. Sample A also shows evidence of voltage-dependent current collection (VDCC) and/or shunting, which is common in ultrathin CIGS solar cells. Such problems are explained in more detail elsewhere [4]. As such, the reference sample (A) has a low fill factor (FF), which is recovered by the passivation reference (B), with shunts mitigation by the passivation layer. We observe that sample D features the highest values of V_{oc}, FF, and efficiency, reaching an average light to power conversion efficiency of 9.6%. Such value is 4.2% (abs) higher than the reference sample and 2.4% (abs) higher than the passivation reference. The V_{oc} value of sample D is 24 mV higher than the passivation reference; hence, the passivation effect is still present and reinforced. Furthermore, there seems to be a J_{sc} improvement of 0.25 mA/cm2, which may be related to an increased reflection achieved by the employment of the tantalum material and that will be discussed further in the text. To demonstrate the importance of the Mo second layer deposited in the line contacts, we also produced sample C that allows Se to be in direct contact with Ta. Sample C shows poor solar cell results, most likely due to diffusion of elements and/or a poor electrical contact between Ta and CIGS, showing the importance of the lift-off process used for sample D. This comparison highlights the importance of a diffusion barrier, also in accordance with previous results [16], [17]. The champion cell of sample D achieved an efficiency value of 10.0%. Moreover, sample D shows an excellent diode-like behavior, with the lowest dark current (J_0) value ($\sim 4 \times 10^{-6}$ mA/cm2), and no evidence of either shunting, seen by the high shunt resistance value, or roll-over effects, which is demonstrated by its high FF value (~70%).

C. Optical Simulations

To better understand the optical gains of using Ta underneath the passivation layer, we will proceed with an optical simulation of the novel stack, shown in Fig. 1, and compare it with the EQE results presented in Fig. 7 for the most important samples identified previously (A, B, and D). It is noted that the optical simulations performed do not account for electrical losses, light scattering in grain boundaries, doping and compositional CIGS variations, interface smearing, just to name a few parameters that influence real devices. Therefore, a difference is expected between the simulated values and the measured ones. Nonetheless, the optical simulations presented in Fig. 8 are in good agreement with

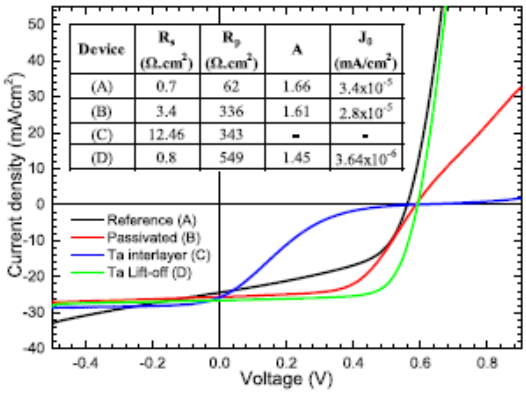

Fig. 6. Illuminated *J–V* curves of the highest V_{oc} device for all samples. The diode parameters are found on the inset table.

TABLE III
J–V VALUES AVERAGES AND STANDARD DEVIATION OF TWELVE DEVICES FOR EACH SUBSTRATE TYPE

Sample	V_{oc} (mV)	EQE corrected J_{sc} (mA/cm^2)	FF (%)	Eff (%)
(A)	535 ± 11 (560)	21.37 ± 0.32 (21.82)	47.5 ± 4.6 (49.9)	5.4 ± 0.7 (6.4)
(B)	558 ± 23 (586)	23.13 ± 0.18 (23.46)	55.2 ± 2.5 (58.5)	7.2 ± 0.7 (8.2)
(C)	519 ± 41 (579)	24.35 ± 0.71 (24.96)	14.5 ± 2.0 (15.7)	1.8 ± 0.2 (2.2)
(D)	582 ± 5 (591)	23.38 ± 0.29 (23.59)	68.0 ± 3.4 (71.7)	9.6 ± 0.5 (10.0)

Note. The values in parenthesis are for the highest V_{oc} device.

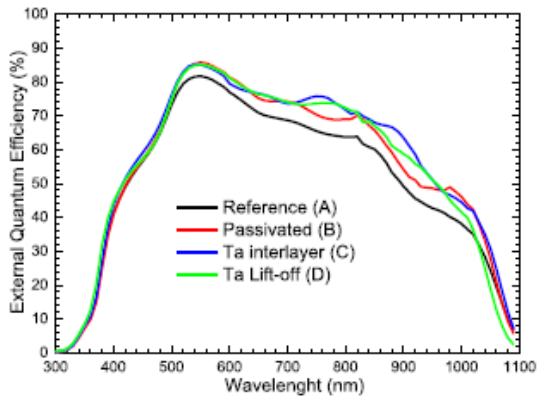

Fig. 7. EQE of the studied samples.

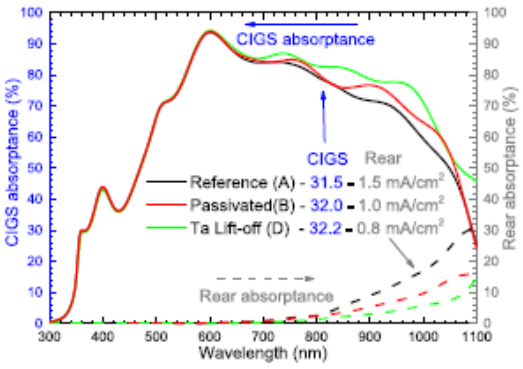

Fig. 8 Simulated CIGS absorptance and rear contact absorptance. For sample A, rear contact absorptance is the Mo absorptance; for sample B, it is Mo+Al_2O_3 absorptance; and for sample D, it is the absorptance of Mo+Ta+Al_2O_3+Mo.

the EQE, even confirming that by adding the passivation layer, an optical effect leads to an increase

in the J_{sc} values. However, the experimental J_{sc} difference between A and B (1.76 mA/cm²) is higher than the simulated J_{sc} difference (0.5 mA/cm²). Such inconsistency is an evidence that part of the J_{sc} increase in sample B is due to electrical passivation and that further passivation optimization is needed. This fact is also highlighted by the observation that in the absorption calculations, there is no difference between the samples behaviour in the short wavelength regime contrary to what is observed in the EQE results, where the samples with passivation present a higher performance even where no optical gains are expected. Such increase in the EQE behavior in all wavelength values, when a passivation layer is added, is observed throughout the literature and needs to be studied in detail.We also note that the experimental J_{sc} difference between B and D (0.25 mA/cm²) is very close to the simulated J_{sc} value (0.2 mA/cm²). This is an indication that the passivation is the same in both substrates and that the simulation is in agreement with the experimental results. Furthermore, by using the novel architecture of sample D, a decrease in parasitic absorption at the rear contact is observed, as shown by the dashed lines in Fig. 8. According to the simulations and with regard to parasitic absorption in the rear contact, sample A has a J_{sc} loss of 1.53 mA/cm² in the Mo layer, sample B has a J_{sc} loss of 1.03 mA/cm2 in the Mo+Al_2O_3 layer and, remarkably, sample D has a J_{sc} loss of 0.86 mA/cm2 in the Mo+Ta+Al_2O_3+Mo. Such solution that allows for a decrease in parasitic absorption at the rear contact is highly interesting even for standard thickness CIGS (2000 nm), where the Mo absorptance can also reach values higher than 1 mA/cm² [27]. We note that for high reflective metals, other losses that are already present here become even more prominent, namely reflection losses, bringing the need to incorporate more advanced light-trapping mechanisms. Nonetheless, even with the improved novel architecture, the J_{sc} values are still far away from simulated values, likely meaning that not only light trapping has to be improved, but also the interface recombination velocity has to be further reduced.

V. Conclusion

In this preliminary study, we introduced a lift-off procedure to fabricate a substrate for thin-film solar cells that decouples the electrical properties from the optical ones. This is accomplished by the electrical contact being made between CIGS and a Mo line contact that uses only a part of the available rear contact area. The rest of the area is passivated by an Al_2O_3 layer, which underneath can have a highly reflective metal layer. Solar cells with the novel lift-off process using Ta as an interlayer show an improvement over both the reference devices and the substrates with Ta without the lift-off process. The 600-nm CIGS thickness solar cells with the new rear contact architecture achieved an average efficiency of 9.6%, which compares to the unpassivated reference of 5.4%.

The proposed novel architecture allows for:

1) a good electrical contact between the CIGS and the rear contact;

2) a beneficial passivation effect;

3) a reduced rear contact light absorptance; and

4) a limitation to the diffusion from and to the absorber layer.

Such architecture allows for a wider ensemble of metals to be used to increase the rear optical reflectance, as most limitations of other metals can now be overcome. Future studies should be focused on studying the effects of this architecture,

improving the lift-off process, and testing highly reflective metals.

REFERENCES

[1] B. Vermang, V. Fjällström, J. Pettersson, P. Salomé, and M. Edoff, "Development of rear surface passivated Cu(In,Ga)Se2 thin film solar cells with nano-sized local rear point contacts," *Sol. Energy Mater. Sol. Cells*, vol. 117, pp. 505–511, Oct. 2013.

[2] J. Krc *et al.*, "Optical confinement in chalcopyrite based solar cells," *Thin Solid Films*, vol. 633, pp. 193–201, Jul. 2017.

[3] J. M. V. Cunha, C. Rocha, C. Vinhais, P. A. Fernandes, and P. M. P. Salomé, "Understanding the AC equivalent circuit response of ultrathin Cu(In,Ga)Se2 solar cells," *IEEE J. Photovolt.*, 2019, doi: 10.1109/JPHOTOV.2019.2927918.

[4] P. M. P. Salomé *et al.*, "Passivation of interfaces in thin film solar cells: Understanding the effects of a nanostructured rear point contact layer," *Adv. Mater. Interfaces*, vol. 5, no. 2, Jan. 2018, Art. no. 1701101.

[5] B. Vermang *et al.*, "Employing Si solar cell technology to increase efficiency of ultra-thin Cu(In,Ga)Se2 solar cells," *Prog. Photovolt. Res. Appl.*, vol. 22, no. 10, pp. 1023–1029, Oct. 2014.

[6] G. Yin *et al.*, "Well-controlled dielectric nanomeshes by colloidal nanosphere lithography for optoelectronic enhancement of ultrathin Cu(In,Ga)Se2 solar cells," *ACS Appl. Mater. Interfaces*, vol. 8, no. 46, pp. 31646–31652, Nov. 2016.

[7] B. Vermang *et al.*, "Rear surface optimization of CZTS solar cells by use of a passivation layer with nanosized point openings," *IEEE J. Photovolt.*, vol. 6, no. 1, pp. 332–336, Jan. 2016.

[8] S. Bose *et al.*, "Optical lithography patterning of SiO2 layers for interface passivation of thin film solar cells," *Sol. RRL*, vol. 2, no. 12, Dec. 2018, Art. no. 1800212.

[9] J. M. V. Cunha *et al.*, "Insulator materials for interface passivation of Cu(In,Ga)Se2 thin films," *IEEE J. Photovolt.*, vol. 8, no. 5, pp. 1313–1319, Sep. 2018.

[10] S. Bose *et al.*, "A morphological and electronic study of ultrathin rear passivated Cu(In,Ga)Se2 solar cells," *Thin SolidFilms*, vol. 671, pp. 77–84, Feb. 2019.

[11] S. Choi *et al.*, "Lithographic fabrication of point contact with Al2O3 rearsurface-passivated and ultra-thin Cu(In,Ga)Se2 solar cells," *Thin Solid Films*, vol. 665, pp. 91–95, Nov. 2018.

[12] G. Yin, P. Manley, and M. Schmid, "Light trapping in ultrathin $CuIn_{1-x}Ga_xSe_2$ solar cells by dielectric nanoparticles," *Sol. Energy*, vol. 163, pp. 443–452, Mar. 2018.

[13] Z. J. Li-Kao *et al.*, "Towards ultrathin copper indium gallium diselenide solar cells: Proof of concept study by chemical etching and gold back contact engineering," *Prog. Photovolt. Res. Appl.*, vol. 20, no. 5, pp. 582–587, Aug. 2012.

[14] N. Naghavi *et al.*, "Ultrathin Cu(In,Ga)Se2 based solar cells," *Thin Solid Films*, vol. 633, pp. 55–60, Jul. 2017.

[15] N. Dahan *et al.*, "Optical approaches to improve the photocurrent generation in Cu(In,Ga)Se2 solar cells with absorber thicknesses down to 0.5 μm," *J. Appl. Phys.*, vol. 112, no. 9, Nov. 2012, Art. no. 094902.

[16] K. Orgassa, H. W. Schock, and J. H. Werner, "Alternative back contact materials for thin film Cu(In,Ga)Se2 solar cells," *Thin Solid Films*, vol. 431–432, pp. 387–391, May 2003.

[17] T. S. Lopes *et al.*, "Rear optical reflection and passivation using a nanopatterned metal/dielectric structure in thin film solar cells," *IEEE J. Photovolt.*, 2019, doi: 10.1109/JPHOTOV.2019.2922323.

[18] P. M. P. Salomé, J. Malaquias, P. A. Fernandes, and A. F. da Cunha, "Mo bilayer for thin film photovoltaics revisited," *J. Phys. D. Appl. Phys.*, vol. 43, no. 34, Sep. 2010, Art. no. 345501.

[19] P. Salomé, V. Fjällström, A. Hultqvist, and M. Edoff, "Na doping of CIGS solar cells using low sodium-doped Mo layer," *IEEE J. Photovolt.*, vol. 3, no. 1, pp. 509–513, Jan. 2013.

[20] J. Lindahl *et al.*, "In line Cu(In,Ga)Se2 co-evaporation for high-efficiency solar cells and modules," *IEEE J. Photovolt.*, vol. 3, no. 3, pp. 1100–1105, Jul. 2013.

[21] P. M. P. Salomé *et al.*, "Cu(In,Ga)Se2 solar cells with varying Na content prepared on nominally alkali-free glass substrates," *IEEE J. Photovolt.*, vol. 3, no. 2, pp. 852–858, Apr. 2013.

[22] P. M. P. Salomé *et al.*, "The effect of high growth temperature on Cu(In,Ga)Se2 thin film solar cells," *Sol. Energy Mater. Sol. Cells*, vol. 123, pp. 166–170, Apr. 2014.

[23] O. Lundberg, M. Edoff, and L. Stolt, "The effect of Ga-grading in CIGS thin film solar cells," *Thin Solid Films*, vol. 480–481, pp. 520–525, Jun. 2005.

[24] B. Vermang *et al.*, "Introduction of Si PERC rear contacting design to boost efficiency of Cu(In,Ga)Se2 solar cells," *IEEE J. Photovolt.*, vol. 4, no. 6, pp. 1644–1649, Nov. 2014.

[25] M. Schmid, "Review on light management by nanostructures in chalcopyrite solar cells," *Semicond. Sci. Technol.*, vol. 32, no. 4, Apr. 2017, Art. no. 043003.

[26] G. Birant, J. de Wild, M. Meuris, J. Poortmans, and B. Vermang, "Dielectric-based rear surface passivation approaches for Cu(In,Ga)Se2 solar cells—A review," *Appl. Sci.*, vol. 9, no. 4, Feb. 2019, Art. no. 677.

[27] B. Bissig *et al.*, "Novel back contact reflector for high efficiency and double-graded Cu(In,Ga)Se2 thin-film solar cells," *Prog. Photovolt. Res. Appl.*, vol. 26, no. 11, pp. 894–900, Nov. 2018.